

# Reversible Hydrogen Storage at Moderate Pressure–Temperature Conditions of C14 Laves Phase Alloys of the $(\text{Ti}_{0.5-x}\text{Zr}_{0.5-x}\text{Nb}_{2x})_1(\text{Mn}_{0.5}\text{Cr}_{0.5})_2$ System

Jéssica Bruna Ponsoni,\* Vinícius Aranda, Walter J. Botta, and Guilherme Zepon



Cite This: *ACS Appl. Energy Mater.* 2025, 8, 8351–8364



Read Online

ACCESS |



Metrics & More



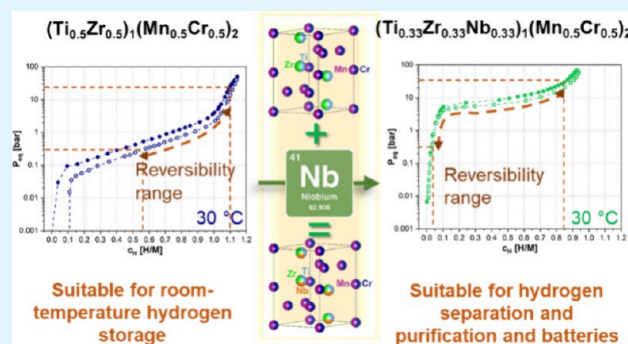
Article Recommendations



Supporting Information

**ABSTRACT:** Hydrogen is increasingly recognized as a crucial alternative to fossil fuels. Solid-state storage utilizing metal hydrides offers a high volumetric density for effective hydrogen storage. In this study, a computational thermodynamic approach was employed to design a C14 Laves phase alloys of the  $(\text{Ti}_{0.5-x}\text{Zr}_{0.5-x}\text{Nb}_{2x})_1(\text{Mn}_{0.5}\text{Cr}_{0.5})_2$  system for hydrogen storage at moderate pressure–temperature. Two alloys were designed, namely,  $(\text{Ti}_{0.5}\text{Zr}_{0.5})_1(\text{Mn}_{0.5}\text{Cr}_{0.5})_2$  and  $(\text{Ti}_{0.33}\text{Zr}_{0.33}\text{Nb}_{0.33})_1(\text{Mn}_{0.5}\text{Cr}_{0.5})_2$ , corresponding to  $x = 0$  and  $x = 0.1667$ , respectively. These alloys were synthesized by arc melting, structurally characterized by different techniques, and had their hydrogen storage properties evaluated in terms of absorption kinetic, pressure–composition–isotherm diagrams, absorption/desorption reversibility, and cycling stability. Both alloys presented hydrogen absorption/desorption reversibility under mild pressure and temperature conditions with excellent cycling stability, making them potential candidates for different hydrogen-related technologies.

**KEYWORDS:** multicomponent alloys, hydrogen storage, reversibility, cycling performance, C14 Laves phase, computational thermodynamics



## 1. INTRODUCTION

In the context of climate change, driven by the extensive use of fossil fuels, hydrogen energy is emerging as a crucial component of a sustainable energy future. The over-dependence on fossil fuels not only depletes finite energy reserves but also exacerbates global warming. In contrast, hydrogen can be efficiently produced via the electrolysis of water and acts as an efficient energy carrier, enabling the effective utilization of renewable and green energy sources, such as solar and wind. Despite the promising potential of a hydrogen economy in promoting a more sustainable energy sector, an efficient and economically viable transition to this hydrogen-based system is heavily contingent upon advancements in hydrogen storage technologies.

Solid-state hydrogen storage offers numerous advantages over gas and liquid storage methods. In chemisorption using metal hydrides (MHs), hydrogen gas dissociates, and hydrogen atoms diffuse within the metal lattice, occupying interstitial sites, eliminating the need for high pressures or cryogenic temperatures depending on the host metal.<sup>1</sup>

MHs might enable the use of hydrogen energy in various stationary and mobile applications such as tanks for solid-state hydrogen storage, heat storage systems, purification systems, fuel cells, and batteries. Each of these applications requires a unique set of properties, which, in turn, necessitates different

MHs. The properties are highly dependent on the composition of the MHs. Multicomponent alloys for hydrogen storage application are mainly constituted by body-centered cubic (BCC) phase alloys, intermetallic compounds, and Mg-based alloys.<sup>2–4</sup>

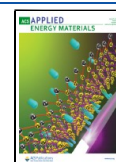
Although intermetallic compounds generally have a lower gravimetric storage capacity compared with BCC or Mg-based alloys, they have garnered significant research interest. These alloys exhibit fast absorption and desorption kinetics and may operate effectively at mild temperature and pressure conditions, and some of them demonstrate excellent cycling stability and storage reversibility, which are critical attributes for practical applications.<sup>5–8</sup> Intermetallic compounds, including AB<sub>3</sub>, AB<sub>2</sub>, A<sub>2</sub>B, and AB-type, are composed of A-type elements, which tend to form hydride phases, and B-type elements, which have a lower affinity for hydrogen. Among these, the C14 Laves phase is the most common intermetallic

Received: March 25, 2025

Revised: May 22, 2025

Accepted: May 23, 2025

Published: June 9, 2025



compound, characterized by an AB<sub>2</sub> stoichiometry.<sup>9</sup> In this context, numerous studies are investigating C14 Laves phase systems with diverse properties, particularly focusing on equilibrium pressures across various value ranges for specific applications.

The C14 Laves phase compositions are mainly formed by a combination of the first-series transition metals, such as Ti, V, Cr, Mn, Fe, Co, and Ni, and second-series transition metals, such as Zr and Nb. The partial substitution of elements A and B with the aforementioned elements, along with other transition metals and rare earth elements, in well-established binary and ternary systems like TiMn<sub>2</sub> and Ti–Cr–Mn-based alloys, has been extensively explored as a strategy to discover new compositions and improve the hydrogen storage properties of these alloys.<sup>10–13</sup>

Ma et al.<sup>10</sup> investigated the Ti<sub>1–x</sub>Sc<sub>x</sub>Mn<sub>1.6</sub>V<sub>0.4</sub> alloy system to enhance its hydrogen storage properties through the addition of Sc. Their study revealed that even a small amount of Sc significantly improves both hydrogen activation and storage performance. Guo et al.<sup>11</sup> and Peng et al.<sup>12</sup> studied Ti–Cr–Mn–Fe-based alloys with high plateau pressures for use in double- and three-stage metal hydride hydrogen compressors. Kandavel et al.<sup>13</sup> investigated the substitution of A elements by studying the partial substitution of Ti with Zr in the Ti<sub>1.1</sub>CrMn alloy, focusing on automotive applications. Their findings demonstrated that increasing the Zr content reduced the equilibrium hydrogen sorption pressure plateau, enhanced absorption kinetics, and improved the hydrogen storage capacity. On the B side, to enhance the hydrogen storage performance of the alloys, transition metals like Fe, Co, Ni, V, and Cu are used to partially substitute Cr or Mn.<sup>14–16</sup> Li et al.<sup>17</sup> studied Ti<sub>0.8</sub>Zr<sub>0.2</sub>Mn<sub>0.9</sub>Cr<sub>0.6</sub>V<sub>0.3</sub>M<sub>0.2</sub> (M = Fe, Ni, Co) alloys, examining how these elements affect the plateau pressures, hysteresis, kinetics, and overall hydrogen storage performance of the alloys.

Following these observations and aiming to improve the modeling of alloys, a comprehensive strategy to design C14 Laves phase alloys for hydrogen storage applications assisted by computational thermodynamic was conducted by Ponsoni et al.<sup>18</sup> They focused on finding C14 Laves phase alloys based on high-throughput calculations of electronic and geometrical factors (valence electron concentration, VEC; atomic radius ratio between A and B elements,  $r_A/r_B$ ; and atomic size mismatch,  $\delta$ ) and CALPHAD calculations of these alloys. Furthermore, the design strategy reported by Ponsoni et al.<sup>18</sup> presents a thermodynamic model to calculate pressure–composition–temperature (PCT) diagrams for the C14 Laves phase alloys. This model is a further development of the thermodynamic model first proposed by Zepon et al.<sup>19</sup> for calculating PCT diagrams for multicomponent BCC alloys.

This work aimed to develop C14 Laves phase alloys of the (Ti<sub>0.5–x</sub>Zr<sub>0.5–x</sub>Nb<sub>2x</sub>)<sub>1</sub>(Mn<sub>0.5</sub>Cr<sub>0.5</sub>)<sub>2</sub> system that can operate under moderate pressure–temperature conditions. The starting composition is the (Ti<sub>0.5</sub>Zr<sub>0.5</sub>)<sub>1</sub>(Mn<sub>0.5</sub>Cr<sub>0.5</sub>)<sub>2</sub> alloy ( $x = 0$ ). The partial substitution of Ti and Zr by Nb was proposed as a strategy to increase the equilibrium pressure of the alloys since Nb is an A-type element with lower hydrogen affinity when compared to both Ti and Zr. By adjusting the composition of the alloy by Nb addition, the hydrogen storage properties of the alloy are changed, allowing its use in different applications.

## 2. EXPERIMENTAL PROCEDURE

**2.1. Alloy Designing via the Thermodynamic Computational Approach.** A design strategy developed by Ponsoni et al.<sup>18</sup> was employed to select the alloys of the (Ti<sub>0.5–x</sub>Zr<sub>0.5–x</sub>Nb<sub>2x</sub>)<sub>1</sub>(Mn<sub>0.5</sub>Cr<sub>0.5</sub>)<sub>2</sub> system aiming to compositions that could operate at moderate pressure–temperature conditions.

The design via thermodynamic computational approach reported by Ponsoni et al.<sup>18</sup> enables the selection of C14 Laves phase alloys based on high-throughput calculations of electronic and geometrical factors including VEC,  $r_A/r_B$ , and  $\delta$ , combined with CALPHAD calculations (Thermo-Calc software and TCHEAS database). Furthermore, the design approach also includes a thermodynamic model for the calculations of pressure–composition–isotherm (PCI) curves of C14 Laves phase alloys.<sup>18</sup>

The calculations of electronic and geometrical factors have been used to predict the formation and stability of the multicomponent Laves phase.<sup>20,21</sup> The Thermo-Calc software and TCHEAS database provided the platform for implementing the CALPHAD method to calculate the equilibrium phases of the designed alloys.<sup>7,22</sup>

These computational tools allow effective prediction of phase formation and how hydrogen equilibrium pressures vary with composition prior to the experimental measurements, reducing the number of experiments needed to find alloys with the desired characteristics.

The C14 Laves phase has a hexagonal crystal structure, belonging to space group  $P6_3/mmc$ . Each unit cell contains 12 atoms, corresponding to four AB<sub>2</sub> formula units. The A-type atoms occupy the 4f (A1) Wyckoff position, while the B-type atoms are located at the 2a (B1) and 6h (B2) Wyckoff positions. In addition, the C14-type Laves phase contains three distinct types of tetrahedral interstitial sites: A<sub>2</sub>B<sub>2</sub>, AB<sub>3</sub>, and B<sub>4</sub>. The structure features 12 equiv A<sub>2</sub>B<sub>2</sub> sites, four equivalent AB<sub>3</sub> sites, and one B<sub>4</sub> site per formula unit, amounting to a total of 68 tetrahedral interstitial sites per unit cell.

The thermodynamic model considers a hydrogen–metal system under para-equilibrium (PE) conditions, which are prevalent for hydrogen storage applications at low or moderate temperatures. In this condition, metal atoms are considered “frozen”, exhibiting limited mobility and negligible long-range diffusion, while hydrogen atoms remain mobile. Achieving PE requires equality of the chemical potentials of metal and hydrogen atoms in the coexisting phases.

The chemical potential of the C14 phase is given by eq 1, and the hydrogen chemical potential of H<sub>2</sub> gas per mol of hydrogen atom is given by eq 2.

$$\mu_{\text{H}}^{\text{C14}}(c_{\text{H}}) = \frac{d\Delta G_{\text{m}}(c_{\text{H}})}{dc_{\text{H}}} \quad (1)$$

$$\mu_{\text{H}}^{\text{H}_2} = \frac{1}{2}RT \ln \left( \frac{P_{\text{H}_2}}{p^0} \right) \quad (2)$$

where  $p^0 = 1$  atm is the reference state. Therefore, to determine the hydrogen concentration in solid solution in a C14 Laves phase for a given hydrogen pressure and ( $P_{\text{H}_2}$ ) and a given temperature, both the hydrogen chemical potential of the C14 Laves and the hydrogen chemical potential of H<sub>2</sub> gas must be the same, i.e.,  $\mu_{\text{H}}^{\text{C14}} = \mu_{\text{H}}^{\text{H}_2}$ . Some assumptions regarding the enthalpy and entropy variations are made to calculate  $\Delta G_{\text{m}}(c_{\text{H}})$ , which are detailed in ref 18. In summary, the PCI curves can be calculated using eq 3.

$$\ln \left( \frac{P_{\text{H}_2}}{p^0} \right) = \frac{2}{RT} \left[ h_{\text{C14}} - T \left[ -R \ln \left( \frac{c_{\text{H}}}{1 - c_{\text{H}}} \right) - \frac{S_{\text{H}_2}^0}{2} \right] \right] \quad (3)$$

where  $p^0 = 1$  atm is the reference state,  $P_{\text{H}_2}$  is a given hydrogen pressure,  $R$  is the ideal gas constant, and  $T$  is a given absolute temperature.  $c_{\text{H}} = \frac{n_{\text{H}}}{n_{\text{M}}}$  is the amount of hydrogen in the phase, where  $n_{\text{H}}$  and  $n_{\text{M}}$  are the number of mols of hydrogen and metal atoms in the phase, respectively.  $S_{\text{H}_2}^0$  is the standard entropy of H<sub>2</sub> gas, which is given by eq 4.<sup>19</sup>

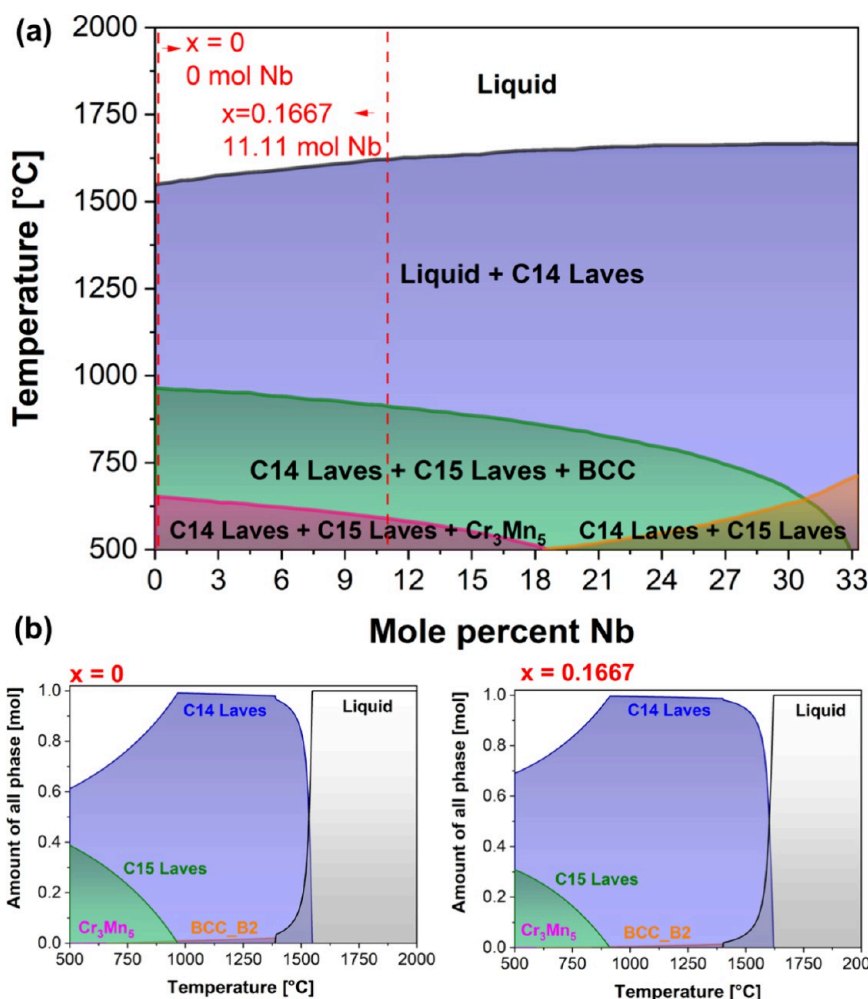


**Figure 1.** (a) Phase diagram as a function of mole percent of Nb calculated by CALPHAD for the  $(\text{Ti}_{0.5-x}\text{Zr}_{0.5-x}\text{Nb}_{2x})_1(\text{Mn}_{0.5}\text{Cr}_{0.5})_2$  system. (b) Amount of equilibrium phases as a function of temperature calculated for  $(\text{Ti}_{0.5-x}\text{Zr}_{0.5-x}\text{Nb}_{2x})_1(\text{Mn}_{0.5}\text{Cr}_{0.5})_2$  with  $x = 0$  and  $x = 0.1667$ .

$$S^0(\text{H}_2) = A \ln(t) + Bt + \frac{Ct^2}{2} + \frac{Dt^3}{3} + \frac{Et^{-2}}{2} + G \left[ \frac{J}{\text{mol of H}_2} \right] \quad (4)$$

where  $t = T(\text{K})/1000$ ,  $A = 33.066178$ ,  $B = -11.363417$ ,  $C = 11.432816$ ,  $D = -2.772874$ ,  $E = -0.158558$ , and  $G = 172.707974$ . It is worth noting that eq 4 is only valid between 298 and 1000 K.

$h_{\text{C14}}$  is the hydrogen partial molar enthalpy of the C14 Laves phase, a term of the  $\Delta H_m(c_H)$  equation, and is described as eq 5.

$$h_{\text{C14}} = \frac{1}{2} \sum_i c_i^A \Delta H_i^\infty + \frac{1}{2} \sum_i c_i^B \Delta H_i^\infty \quad (5)$$

where  $c_i^A$  is the atomic fraction of element  $i$  in the A sublattice, and  $c_i^B$  is the atomic fraction of element  $i$  in the B sublattice (therefore,  $\sum_i c_i^A = \sum_i c_i^B = 1$ ).  $\Delta H_i^\infty$  is the enthalpy of a hydrogen solution in element  $i$  at infinite dilution. Experimental values of  $\Delta H_i^\infty$  are reported by Griessen and Riesterer,<sup>23</sup> and the values for the elements of the studied alloys in kJ/mol H are  $\Delta H_{\text{Ti}}^\infty = -52$ ,  $\Delta H_{\text{Zr}}^\infty = -52$ ,  $\Delta H_{\text{Nb}}^\infty = -35$ ,  $\Delta H_{\text{Mn}}^\infty = 1$ , and  $\Delta H_{\text{Cr}}^\infty = 28$ .

**2.2. Sample Production.** The  $(\text{Ti}_{0.5}\text{Zr}_{0.5})_1(\text{Mn}_{0.5}\text{Cr}_{0.5})_2$  and  $(\text{Ti}_{0.33}\text{Zr}_{0.33}\text{Nb}_{0.33})_1(\text{Mn}_{0.5}\text{Cr}_{0.5})_2$  alloys were selected using the CALPHAD method and thermodynamic model to calculate PCI curves. The alloys were produced from pure elements (purity >99%) by arc melting under an inert argon atmosphere in an electric arc furnace (Arc Melter MAM 1 from Edmund Buehler). Titanium getters were melted previous to the alloys to reduce the oxygen content in the melting chamber. To ensure chemical homogeneity, the samples weighing approximately 10 g were turned over and

remelted at least three times. The as-cast ingot samples were stored in an argon-filled MBRAUM glovebox ( $\text{H}_2\text{O}$  and  $\text{O}_2$  levels below 1 ppm). For the sake of clarity, the subscript values represent the atomic fractions of each element. In terms of mole percent, as shown in some graphs and tables, the values are  $\text{Ti}_{16.67}\text{Zr}_{16.67}\text{Mn}_{33.33}\text{Cr}_{33.33}$  and  $\text{Ti}_{11.11}\text{Zr}_{11.11}\text{Nb}_{11.11}\text{Mn}_{33.33}\text{Cr}_{33.33}$ .

**2.3. Structural Characterization.** The structural characterization was conducted via X-ray diffraction (XRD) using a Bruker D8 Advance Eco diffractometer with  $\text{K}\alpha\text{Cu}$  radiation (1.5406 Å). The data were collected in the  $2\theta$  range between 15 and  $90^\circ$  with a step width of  $0.02^\circ$ . The XRD profiles were analyzed by a Rietveld refinement method using GSAS-II software<sup>24</sup> to determine lattice parameters and phase fraction. The chemical composition and homogeneity of the as-cast alloys was evaluated by energy-dispersive spectroscopy (EDX) using an Oxford EDX Detector in a Philips XL-30 FEG scanning electron microscope (SEM). For the XRD analysis, the as-cast ingot samples were crushed into powder inside an argon-filled MBRAUM glovebox by using an agate mortar and pestle.

**2.4. Hydrogen Storage Characterization.** For the hydrogen storage property evaluation, the as-cast ingot samples were crushed into powder inside a glovebox and loaded into a Sieverts-type apparatus (Setaram PCT Pro-version E&E). Approximately 1 g of the powdered alloys were loaded into the sample holder. For the first hydrogen absorption kinetic measurement, the  $(\text{Ti}_{0.5}\text{Zr}_{0.5})_1(\text{Mn}_{0.5}\text{Cr}_{0.5})_2$  and  $(\text{Ti}_{0.33}\text{Zr}_{0.33}\text{Nb}_{0.33})_1(\text{Mn}_{0.5}\text{Cr}_{0.5})_2$  samples were exposed to hydrogen at 25 and 38 bar, respectively, at  $25^\circ\text{C}$ . The samples were also subjected to a heat treatment at  $390^\circ\text{C}$  under a dynamic vacuum for 2 h before a second kinetic measurement



to avoid any remaining hydrogen from the first measurement and ensure a good hydrogenation. Pressure–composition–isotherm (PCI) were obtained at 30, 60, and 90 °C for the  $(\text{Ti}_{0.5}\text{Zr}_{0.5})_1(\text{Mn}_{0.5}\text{Cr}_{0.5})_2$  alloy and 30, 50, and 70 °C for the  $(\text{Ti}_{0.33}\text{Zr}_{0.33}\text{Nb}_{0.33})_1(\text{Mn}_{0.5}\text{Cr}_{0.5})_2$  alloy. The absorption and desorption PCI curves were recorded by applying doses of hydrogen up to a maximum pressure of 80 bar. After each measurement, the sample was exposed to a dynamic vacuum for a few minutes at the current temperature.

For cycling experiments, the absorption kinetics for the  $(\text{Ti}_{0.33}\text{Zr}_{0.33}\text{Nb}_{0.33})_1(\text{Mn}_{0.5}\text{Cr}_{0.5})_2$  alloy was carried out under initial hydrogen pressures of 36 bar (reservoir volume of 13 cm<sup>3</sup>, approximately). The desorption kinetic measurements were carried out by reducing the hydrogen pressure in the sample to values of under 1 bar. Therefore, the sample was not exposed to a dynamic vacuum during the desorption kinetics measurements. The hydrogen gas was expanded into the apparatus's largest reservoir volume (approximately 1040 cm<sup>3</sup>) to reach pressures below 1 bar. The alloy was subjected to a maximum of 50 cycles of hydrogen absorption and desorption without air or dynamic vacuum exposure. The cycling behavior of the  $(\text{Ti}_{0.5}\text{Zr}_{0.5})_1(\text{Mn}_{0.5}\text{Cr}_{0.5})_2$  alloy was evaluated under three conditions. This included testing with an initial hydrogen pressure of 21 bar over 20 cycles, similar to the conditions under which the  $(\text{Ti}_{0.33}\text{Zr}_{0.33}\text{Nb}_{0.33})_1(\text{Mn}_{0.5}\text{Cr}_{0.5})_2$  alloy was evaluated. Additionally, the alloy was subjected to vacuum and temperature variations, with each condition also using an initial hydrogen pressure of 21 bar.

Structural characterizations by XRD and SEM were performed on samples subjected to the first and last absorption/desorption cycles. In this way, it was possible to relate the cycling behavior to possible structural and compositional changes of the alloys throughout the cycles.

### 3. RESULTS

**3.1. Alloy Designing via the Thermodynamic Computational Approach.** Figure 1 shows the phase diagram as a function of mole percent of Nb calculated by CALPHAD for the  $(\text{Ti}_{0.5-x}\text{Zr}_{0.5-x}\text{Nb}_{2x})_1(\text{Mn}_{0.5}\text{Cr}_{0.5})_2$  system and the amount of equilibrium phases as a function of temperature calculated for the  $(\text{Ti}_{0.5-x}\text{Zr}_{0.5-x}\text{Nb}_{2x})_1(\text{Mn}_{0.5}\text{Cr}_{0.5})_2$  with  $x = 0$  and  $x = 0.1667$ .

The thermodynamic calculations show that under equilibrium conditions, the entire alloy system from 0 mol % Nb ( $x = 0$ , i.e.,  $(\text{Ti}_{0.5}\text{Zr}_{0.5})_1(\text{Mn}_{0.5}\text{Cr}_{0.5})_2$ ) to 33.33 mol % Nb ( $x = 0.5$ , i.e.,  $(\text{Nb})_1(\text{Mn}_{0.5}\text{Cr}_{0.5})_2$ ) solidifies as a primary C14 Laves phase. Therefore, any alloy selected in this system should present the desired Laves phase in its structure.

The starting composition was the  $(\text{Ti}_{0.5}\text{Zr}_{0.5})_1(\text{Mn}_{0.5}\text{Cr}_{0.5})_2$  alloy with  $x = 0$ . The values of the VEC,  $r_A/r_B$ , and  $\delta$  of the alloy are shown in Table 1. These electronic and geometric

**Table 1.**  $r_A/r_B$ , VEC, and  $\delta$  of the Selected Alloys

alloy	$r_A/r_B$	VEC	$\delta$
$(\text{Ti}_{0.5}\text{Zr}_{0.5})_1(\text{Mn}_{0.5}\text{Cr}_{0.5})_2$	1.209	6.3	9.7
$(\text{Ti}_{0.33}\text{Zr}_{0.33}\text{Nb}_{0.33})_1(\text{Mn}_{0.5}\text{Cr}_{0.5})_2$	1.194	6.4	9.0

values are within the range of values with the highest incidence of the C14 Laves phase observed in the study reported by Ponsoni et al.<sup>18</sup> of a total of 1208 compositions, i.e.,  $5.8 \leq \text{VEC} \leq 7.0$ ,  $1.1233 \leq r_A/r_B \leq 1.223$ , and  $\delta > 5\%$ . Although these electronic and geometric factors alone are insufficient to explain the formation and stability of the Laves phase, they play an essential role in predicting the Laves phase formation as widely discussed in the literature.<sup>7,20,21</sup> Indeed, CALPHAD shows that the alloy solidifies as a primary C14 Laves phase

(Figure 1). Further, in the final stage of the solidification, the formation of a minor fraction of the BCC phase (approximately 1%) is also predicted as observed for  $x = 0$  in Figure 1b. Upon cooling to lower temperatures, the formation of a C15 Laves phase and other cubic phases is also expected under equilibrium conditions. However, the formation of the cubic phases might be suppressed due to the high cooling rate imposed by the arc melting synthesis process.

Via the reported thermodynamic model developed for C14 Laves phase alloys,<sup>18</sup> the  $h_{\text{C14}}$  was calculated for the compositions from  $x = 0$  to  $x = 0.5$ . Therefore, we are able to calculate the PCI curves at 25 °C and to obtain the hydrogen equilibrium pressures as a function of  $c_H$  for this entire composition range. The calculated PCI curves and hydrogen equilibrium pressures are presented in Figure S1 and Table S1, respectively, in the Supporting Information.

Figure 2 illustrates the hydrogen equilibrium pressures at  $c_H = 0.5$  for the alloys in the  $(\text{Ti}_{0.5-x}\text{Zr}_{0.5-x}\text{Nb}_{2x})_1(\text{Mn}_{0.5}\text{Cr}_{0.5})_2$

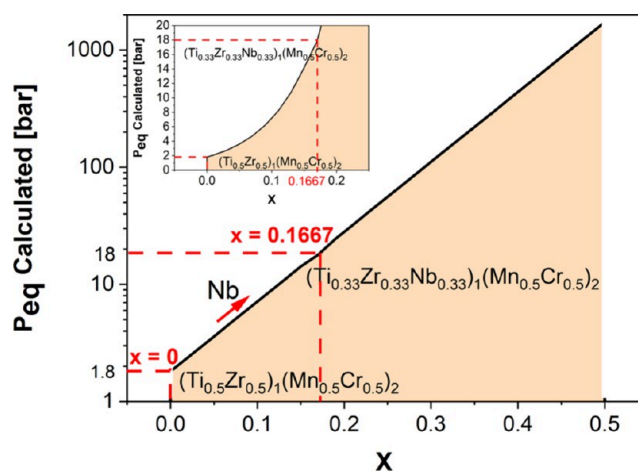


**Figure 2.** Calculated equilibrium pressures for the selected  $(\text{Ti}_{0.5-x}\text{Zr}_{0.5-x}\text{Nb}_{2x})_1(\text{Mn}_{0.5}\text{Cr}_{0.5})_2$  alloys at 25 °C from  $x = 0$  (0 mol % Nb, i.e.,  $(\text{Ti}_{0.5}\text{Zr}_{0.5})_1(\text{Mn}_{0.5}\text{Cr}_{0.5})_2$ ) to  $x = 0.5$  (33.33 mol % Nb, i.e.,  $(\text{Nb})_1(\text{Mn}_{0.5}\text{Cr}_{0.5})_2$ ).

system over a wide composition range. For  $x = 0$ ,  $(\text{Ti}_{0.5}\text{Zr}_{0.5})_1(\text{Mn}_{0.5}\text{Cr}_{0.5})_2$  alloy, the calculated equilibrium pressure at  $c_H = 0.5$  is 1.8 bar, whereas for  $x = 0.5$ ,  $(\text{Nb})_1(\text{Mn}_{0.5}\text{Cr}_{0.5})_2$  alloy, the calculated pressure exceeds 1700 bar. The  $(\text{Ti}_{0.5}\text{Zr}_{0.5})_1(\text{Mn}_{0.5}\text{Cr}_{0.5})_2$  alloy is characterized by  $h_{\text{C14}} = -18.75 \text{ kJ mol}^{-1} \text{ H}$  and the  $(\text{Nb})_1(\text{Mn}_{0.5}\text{Cr}_{0.5})_2$  alloy by  $h_{\text{C14}} = -10.42 \text{ kJ mol}^{-1} \text{ H}$ .

The Nb-containing alloy  $(\text{Ti}_{0.33}\text{Zr}_{0.33}\text{Nb}_{0.33})_1(\text{Mn}_{0.5}\text{Cr}_{0.5})_2$ ,  $x = 0.1667$ , was chosen due to its significantly higher calculated hydrogen equilibrium pressure, which is an order of magnitude higher than that of the starting composition. The  $(\text{Ti}_{0.33}\text{Zr}_{0.33}\text{Nb}_{0.33})_1(\text{Mn}_{0.5}\text{Cr}_{0.5})_2$  alloy is characterized by  $h_{\text{C14}} = -15.92 \text{ kJ mol}^{-1} \text{ H}$ . This alloy exhibited an equilibrium pressure of 18 bar, a value that also facilitates hydrogen desorption at room temperature and is still considered moderate for the targeted applications of this study.

The values of VEC,  $r_A/r_B$ , and  $\delta$  for the  $(\text{Ti}_{0.33}\text{Zr}_{0.33}\text{Nb}_{0.33})_1(\text{Mn}_{0.5}\text{Cr}_{0.5})_2$  alloy are shown in Table 1. These values also lie within the range associated with the highest incidence of the C14 Laves phase.<sup>18</sup> This Nb-containing composition is highlighted by the red dashed line in Figure 1 ( $x = 0.1667 = 11.11 \text{ mol}$  of Nb).

The mole fraction of equilibrium phases as a function of temperature, calculated by CALPHAD, also shown in Figure 1, indicates that the alloy solidifies primarily as the C14 Laves phase. Similar to the  $(\text{Ti}_{0.5}\text{Zr}_{0.5})_1(\text{Mn}_{0.5}\text{Cr}_{0.5})_2$  alloy, the final stage of solidification predicts the formation of a small fraction of the BCC phase. Additionally, the formation of other cubic phases is predicated during cooling. However, the high cooling rate imposed by the synthesis method used, as previously discussed, may suppress the formation of these secondary phases.

**3.2. Structural Characterization.** Figure 3 shows the XRD patterns with the respective Rietveld refinement results

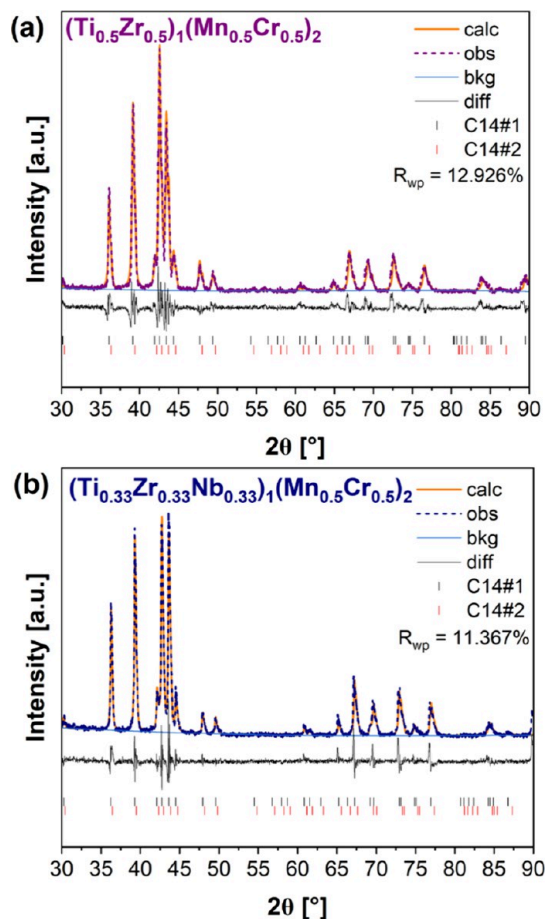


**Figure 3.** Rietveld refinement of the XRD pattern of the as-cast (a)  $(\text{Ti}_{0.5}\text{Zr}_{0.5})_1(\text{Mn}_{0.5}\text{Cr}_{0.5})_2$  and (b)  $(\text{Ti}_{0.33}\text{Zr}_{0.33}\text{Nb}_{0.33})_1(\text{Mn}_{0.5}\text{Cr}_{0.5})_2$  alloys indicating that the samples formed a C14 Laves phase structure.

for the as-cast  $(\text{Ti}_{0.5}\text{Zr}_{0.5})_1(\text{Mn}_{0.5}\text{Cr}_{0.5})_2$  (Figure 3a) and  $(\text{Ti}_{0.33}\text{Zr}_{0.33}\text{Nb}_{0.33})_1(\text{Mn}_{0.5}\text{Cr}_{0.5})_2$  (Figure 3b) alloys, confirming that the alloys have a single C14 Laves phase structure. No reflections from a secondary phase, such as BCC or B2, can be observed. The crystal structures of the hexagonal C14 Laves phases of the studied alloys are shown in Table S2 and Figure S2, respectively, in the Supporting Information. These crystal structures were used in the Rietveld refinement procedure. Figure 3 illustrates that the as-cast structures of the  $(\text{Ti}_{0.5}\text{Zr}_{0.5})_1(\text{Mn}_{0.5}\text{Cr}_{0.5})_2$  and  $(\text{Ti}_{0.33}\text{Zr}_{0.33}\text{Nb}_{0.33})_1(\text{Mn}_{0.5}\text{Cr}_{0.5})_2$  alloys could be described using two distinct C14 Laves phases, hereafter termed C14#1 and C14#2. The lattice parameters and phase fractions of both C14 Laves phases, as determined by Rietveld refinement, are listed in Table 2. Although the

**Table 2.** Lattice Parameters and Phase Fractions of the C14 Laves Phases Determined by Rietveld Refinement for the  $(\text{Ti}_{0.5}\text{Zr}_{0.5})_1(\text{Mn}_{0.5}\text{Cr}_{0.5})_2$  and  $(\text{Ti}_{0.33}\text{Zr}_{0.33}\text{Nb}_{0.33})_1(\text{Mn}_{0.5}\text{Cr}_{0.5})_2$  Alloys

alloy	phases	lattice parameters (Å)	phase fraction (wt %)
$(\text{Ti}_{0.5}\text{Zr}_{0.5})_1(\text{Mn}_{0.5}\text{Cr}_{0.5})_2$	C14#1	$a = 4.9742$ $c = 8.1628$	84.2
	C14#2	$a = 4.9399$ $c = 8.1111$	15.8
	C14#1	$a = 4.9510$ $c = 8.1347$	86.4
	C14#2	$a = 4.9274$ $c = 8.0929$	13.6

alloys are single-phase, the XRD pattern can only be accurately fitted using two C14 Laves phases with very similar lattice parameters. This approach is necessary to account for compositional microsegregation, which will be discussed in detail below.

Both alloys presented a slight broadening of the C14 Laves phase reflections, possibly related to a minor deviation in the chemical composition due to segregation during solidification. A gradient in the chemical composition caused by segregation can also lead to a small gradient in the lattice parameters of the C14 Laves phase, resulting in peak broadening.

The deviation in the composition throughout the bulk of the C14 Laves phase alloys synthesized by arc melting is commonly observed due to the dendritic microstructure resulting from this casting process.<sup>7,25,26</sup> In this way, the alloy microstructure was further investigated by SEM equipped with EDX, and the results are shown in Figures 4 and 5.

Indeed, the as-cast samples presented a dendritic microstructure, as shown in the SEM-BSE images. Further, the SEM-BSE image, which is sensitive to differences in atomic number, reveals that there is a difference in composition between the dendritic and interdendritic regions. Figure 4 also shows the corresponding EDX elemental maps of the selected region. EDX analyses were carried out in mapping mode in all the selected regions and as point mode in the two areas: at the interdendritic regions and in the middle of dendrites. The results of the overall chemical composition and the chemical composition in the dendritic and interdendritic regions are presented in Table 3.

One can see that the overall composition of the alloy is very close to the nominal one. Ti and Zr are not homogeneously distributed between the dendritic and interdendritic regions, resulting from segregation during solidification. Furthermore, although the Mn and Cr elements appear to be uniformly distributed in the EDX maps, the point EDX analyses showed that there is a small variation of these elements between the dendritic and interdendritic regions. The chemical composition measured in the interdendritic region is slightly richer in Ti and Mn and poorer in Zr and Cr. In contrast, the chemical composition measured in the middle of the dendrites is slightly richer in Zr and Cr and poorer in Ti and Mn.

The SEM-BSE image and corresponding EDX elemental maps of the as-cast  $(\text{Ti}_{0.33}\text{Zr}_{0.33}\text{Nb}_{0.33})_1(\text{Mn}_{0.5}\text{Cr}_{0.5})_2$  alloy are shown in Figure 5. This alloy follows the same behavior observed in the previous alloy regarding the microstructure and elements distribution.



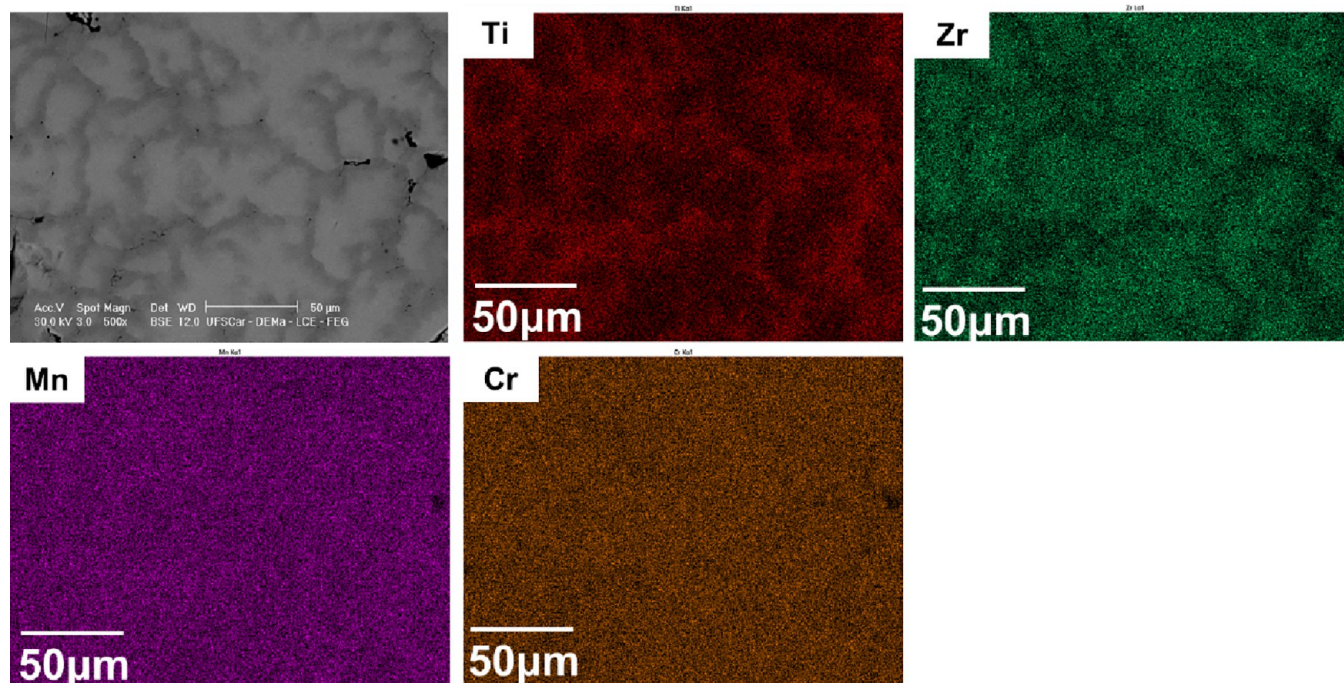


**Figure 4.** SEM-BSE image and corresponding EDX elemental maps of the as-cast  $(\text{Ti}_{0.5}\text{Zr}_{0.5})_1(\text{Mn}_{0.5}\text{Cr}_{0.5})_2$  alloy.

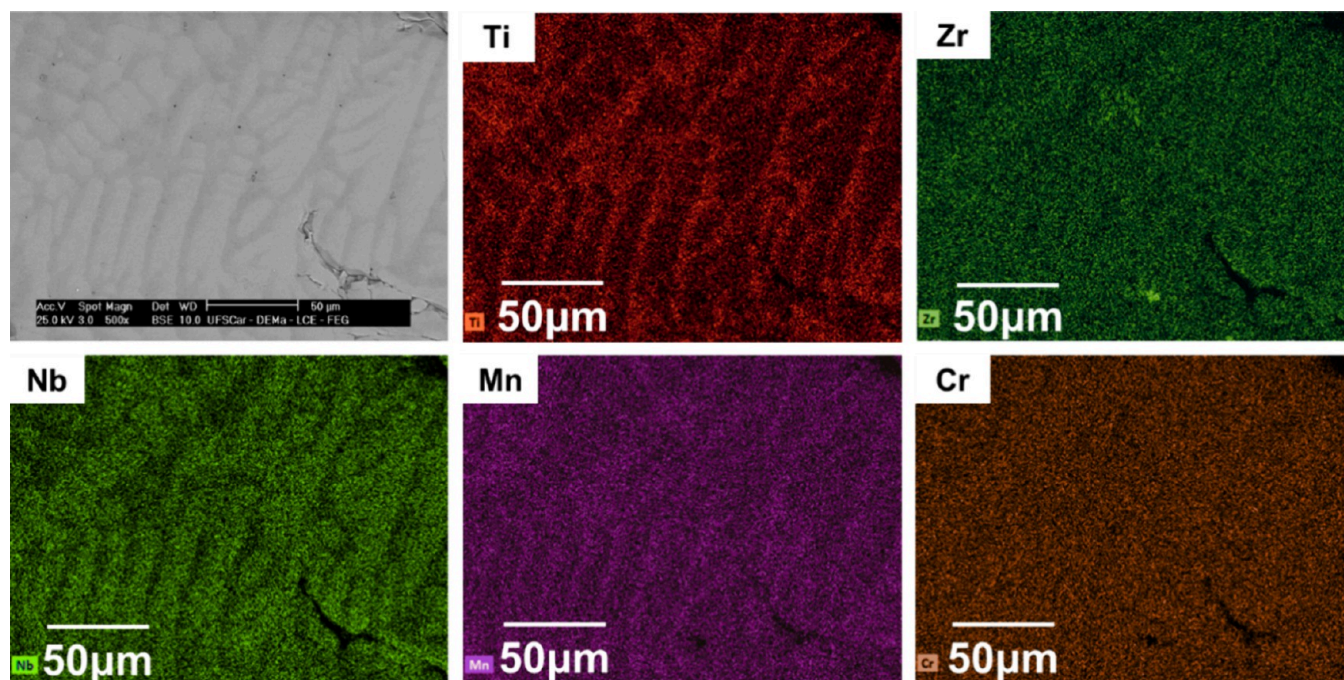


**Figure 5.** SEM-BSE image and corresponding EDX elemental maps of the as-cast  $(\text{Ti}_{0.33}\text{Zr}_{0.33}\text{Nb}_{0.33})_1(\text{Mn}_{0.5}\text{Cr}_{0.5})_2$  alloy.

However, as seen in Table 3, the resulting overall compositions slightly differ from the nominal one in relation to Nb. This difference might be related to a poor homogenization of the elements during the synthesis, which is directly related to the different melting points of the elements. Nb has a melting point equal to 2477  $^{\circ}\text{C}$ , higher than the other alloy elements (Ti = 1668  $^{\circ}\text{C}$ , Zr = 1855  $^{\circ}\text{C}$ , Mn = 1246  $^{\circ}\text{C}$ , and Cr = 1907  $^{\circ}\text{C}$ ), which lead to a small unmelted piece of Nb that however could be removed from the sample when the alloy was crushed into powder. Beyond that, no substantial influence on the alloy crystal structure was

observed in the XRD pattern (Figure 3b). Like the alloy without Nb, the chemical composition measured in the interdendritic region is richer in Ti and Mn and poorer in Zr, Nb, and Cr. The chemical composition measured in the middle of the dendrites is richer in Zr, Nb, and Cr and poorer in Ti and Mn.

Minor deviations in the chemical composition across different regions of the alloy are likely responsible for the slight broadening of the C14 Laves phase reflections observed, as mentioned above, as well as for the need to use two distinct C14 phases (termed C14#1 and C14#2) to accurately fit the



**Table 3. Chemical Composition of the  $(\text{Ti}_{0.5}\text{Zr}_{0.5})_1(\text{Mn}_{0.5}\text{Cr}_{0.5})_2$  and  $(\text{Ti}_{0.33}\text{Zr}_{0.33}\text{Nb}_{0.33})_1(\text{Mn}_{0.5}\text{Cr}_{0.5})_2$  Alloy Determined by SEM-EDX**

(Ti <sub>0.5</sub> Zr <sub>0.5</sub> ) <sub>1</sub> (Mn <sub>0.5</sub> Cr <sub>0.5</sub> ) <sub>2</sub>	chemical composition in at % of the as-cast alloys				
	Ti	Zr	Mn	Cr	
nominal	16.7	16.7	33.3	33.3	
overall	18.5 ± 0.4	17.1 ± 0.2	31.4 ± 0.2	33.0 ± 0.3	
dendritic	13.2 ± 1.1	21.6 ± 1.1	29.7 ± 0.4	35.6 ± 0.4	
interdendritic	23.4 ± 2.5	11.9 ± 2.0	34.0 ± 1.1	30.6 ± 1.6	
(Ti <sub>0.33</sub> Zr <sub>0.33</sub> Nb <sub>0.33</sub> ) <sub>1</sub> (Mn <sub>0.5</sub> Cr <sub>0.5</sub> ) <sub>2</sub>	Ti	Zr	Nb	Mn	Cr
nominal	11.1	11.1	11.1	33.3	33.3
overall	14.9 ± 3.4	12.3 ± 1.5	7.9 ± 2.8	30.3 ± 3.0	33.8 ± 2.8
dendritic	10.0 ± 0.1	14.1 ± 0.2	12.2 ± 0.1	25.8 ± 0.1	38.0 ± 0.3
interdendritic	16.3 ± 2.3	11.9 ± 1.3	6.6 ± 1.6	31.6 ± 1.9	32.6 ± 1.7

XRD patterns. More specifically, this necessity arises from the segregation of Zr and Ti: one region of the sample, corresponding to the dendritic area, is richer in Zr, while the interdendritic region is richer in Ti, as previously presented. This behavior is consistent with findings reported in the literature for other C14 Laves phase alloys.<sup>27</sup>

It is worth noting that the Mn content is slightly lower than the nominal one for both alloys, which can be explained by its partial vaporization during the arc melting procedure due to its lower melting and boiling points and higher vapor pressure compared to the other alloying elements.

**3.3. Hydrogen Storage Properties.** **3.3.1. Absorption Kinetics and PCI Measurements.** The hydrogen absorption kinetic measurements of the  $(\text{Ti}_{0.5}\text{Zr}_{0.5})_1(\text{Mn}_{0.5}\text{Cr}_{0.5})_2$  alloy, shown in Figure 6a, were conducted at 25 °C under hydrogen

pressures of 25 bar (first kinetic) and 21 bar (second kinetic). Initially, the alloy was not subjected to any activation procedure. The first absorption measurement (black curve) demonstrated that the alloy absorbed hydrogen rapidly, but with a short incubation time of about 1 min. It then took approximately 5 min to reach its total hydrogen absorption capacity of  $\text{H}/\text{M} \cong 1.13$  (1.90 wt %). In contrast, the second absorption measurement (red curve) showed no noticeable incubation time; the alloy began absorbing hydrogen immediately upon contact with the gas. Additionally, the alloy reached its total hydrogen absorption capacity of  $\text{H}/\text{M} \cong 1.08$  (1.82 wt %) within just a few seconds. It is worth mentioning that between the first and second kinetics measurements, the  $(\text{Ti}_{0.5}\text{Zr}_{0.5})_1(\text{Mn}_{0.5}\text{Cr}_{0.5})_2$  alloy was subjected to dynamic vacuum at room temperature for 1 h to ensure complete H desorption prior the second measurement.

Similar kinetics behavior was observed for some reported alloys, such as  $\text{Ti}_{0.8}\text{Zr}_{0.2}\text{Cr}_{0.75}\text{M}_{1.25}\text{Ce}_{0.02}$ ,<sup>28</sup>  $\text{Ti}_{0.8}\text{Zr}_{0.2}\text{Mn}_{0.9}\text{Cr}_{0.6}\text{V}_{0.3}\text{M}_{0.2}$  ( $\text{M} = \text{Fe}, \text{Ni}, \text{Co}$ ),<sup>17</sup>  $(\text{TiZr})_1(\text{CrMnFeNi})_2$ ,<sup>7</sup> and  $(\text{Ti}_{0.8}\text{Zr}_{0.2})_{1.1}\text{Mn}_{1.2}\text{Cr}_{0.55}\text{Ni}_{0.2}\text{V}_{0.05}$ ,<sup>29</sup> most of them requiring a few minutes to reach the maximum absorption capacity. The study reported by Tu et al.<sup>29</sup> for the  $(\text{Ti}_{0.8}\text{Zr}_{0.2})_{1.1}\text{Mn}_{1.2}\text{Cr}_{0.55}\text{Ni}_{0.2}\text{V}_{0.05}$  alloy clearly shows the decrease in the time for hydrogen absorption over several kinetics measurements. Only in the fourth absorption measurement did the alloy present fast absorption kinetics, requiring only a few seconds to reach the full hydrogen absorption capacity.

The hydrogen absorption and desorption performance of the  $(\text{Ti}_{0.5}\text{Zr}_{0.5})_1(\text{Mn}_{0.5}\text{Cr}_{0.5})_2$  alloy was further evaluated by PCI measurements, as shown in Figure 7a. The measurements were conducted at 30, 60, and 90 °C up to the maximum hydrogen pressure of 80 bar. It is worth mentioning that the same sample was used for the PCI measurements at three different temperatures. After each desorption, with the hydrogen pressure reduced to around 1 bar, the samples were exposed to a dynamic vacuum for a few minutes to ensure that no residual absorbed hydrogen remained.

One can see that the maximum hydrogen uptake at 80 bar decreases as the temperature increases:  $\text{H}/\text{M} = 1.14$  (1.92 wt %),  $\text{H}/\text{M} = 1.07$  (1.81 wt %), and  $\text{H}/\text{M} = 1.01$  (1.70 wt %) for 30, 60, and 90 °C, respectively. For these temperatures, the observed hydrogen equilibrium pressures for the alloy having 0.5 were approximately 0.4, 1.3, and 3.5 bar, respectively. The hydrogen storage capacities observed for the  $(\text{Ti}_{0.5}\text{Zr}_{0.5})_1(\text{Mn}_{0.5}\text{Cr}_{0.5})_2$  alloy in the kinetics and PCI curves are close to the theoretical value of 1.70 wt % calculated

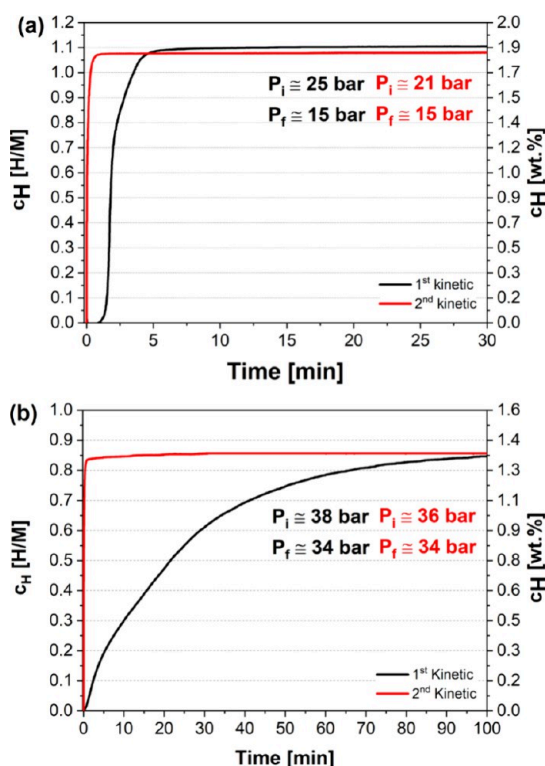


**Figure 6.** Hydrogen absorption kinetics at 25 °C in H/M and wt % for (a)  $(\text{Ti}_{0.5}\text{Zr}_{0.5})_1(\text{Mn}_{0.5}\text{Cr}_{0.5})_2$  and (b)  $(\text{Ti}_{0.33}\text{Zr}_{0.33}\text{Nb}_{0.33})_1(\text{Mn}_{0.5}\text{Cr}_{0.5})_2$  alloys. The first and second kinetics correspond to measurements before and after activation at 390 °C under dynamic vacuum for 2 h.

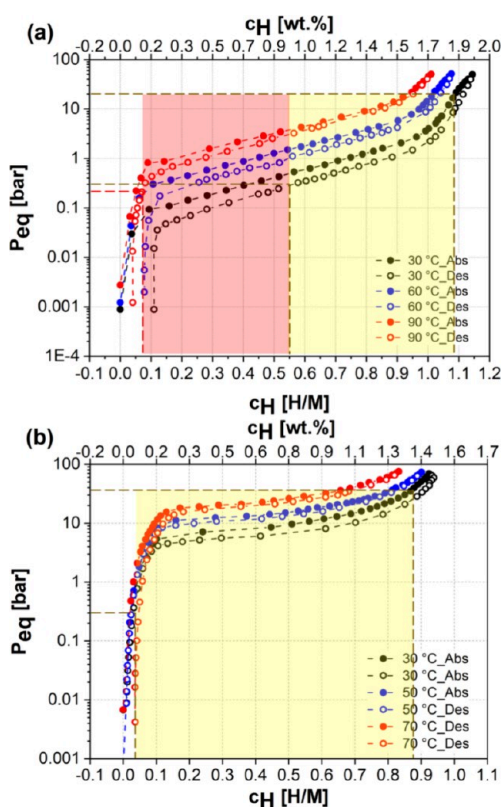


**Figure 7.** PCIs of (a)  $(\text{Ti}_{0.5}\text{Zr}_{0.5})_1(\text{Mn}_{0.5}\text{Cr}_{0.5})_2$  alloy at 30, 60, and 90 °C and (b)  $(\text{Ti}_{0.33}\text{Zr}_{0.33}\text{Nb}_{0.33})_1(\text{Mn}_{0.5}\text{Cr}_{0.5})_2$  alloy at 30, 50, and 70 °C. Highlighted areas indicate pressure and capacity ranges used in cycling tests: in panel (a), yellow for panel (a) and yellow + red for Figure 8; in panel (b), yellow for Figure 9.

considering the formation of an  $\text{AB}_2\text{H}_3$  hydride. Moreover, the PCI curves at the three measured temperatures presented minimal hysteresis.

Although the proposed thermodynamic model enabled a reasonable determination of the equilibrium pressure for the  $(\text{Ti}_{0.5}\text{Zr}_{0.5})_1(\text{Mn}_{0.5}\text{Cr}_{0.5})_2$  alloy, the actual equilibrium pressure was found to be lower than the atmospheric pressure. The PCI revealed a hydrogen equilibrium pressure of approximately 0.43 bar at 30 °C. This characteristic implies incomplete desorption when the hydrogen pressure is released (without applying a vacuum) at 30 °C.

To overcome this barrier to complete desorption, some alternatives were explored in the study. The first strategy included the application of vacuum and temperature-induced desorption measurements, as it will be discussed in Section 3.3.2. The second strategy consisted of designing a new composition,  $(\text{Ti}_{0.33}\text{Zr}_{0.33}\text{Nb}_{0.33})_1(\text{Mn}_{0.5}\text{Cr}_{0.5})_2$ , which presented calculated hydrogen equilibrium 1 order of magnitude higher than that of the starting composition.

Figure 6b shows the hydrogen absorption kinetic curves of the  $(\text{Ti}_{0.33}\text{Zr}_{0.33}\text{Nb}_{0.33})_1(\text{Mn}_{0.5}\text{Cr}_{0.5})_2$  alloy. The analyses were conducted at 25 °C under hydrogen pressures of 38 bar (first kinetic) and 36 bar (second kinetic). Like the  $(\text{Ti}_{0.5}\text{Zr}_{0.5})_1(\text{Mn}_{0.5}\text{Cr}_{0.5})_2$  alloy, this alloy was not subjected to any activation procedures. As can be seen in Figure 6b, the alloy started to absorb hydrogen as soon as it was in contact with the gas; however, it presented slow kinetics. It took approximately 100 min to absorb the total capacity of  $\text{H}/\text{M} \cong 0.86$  (1.38 wt %). Whereas, in the second kinetic measurement

(red curve), it took only a few seconds to reach the total hydrogen absorption capacity of  $\text{H}/\text{M} \cong 0.86$  (1.38 wt %). Notably, the starting alloy displayed a superior maximum storage capacity compared to the Nb-containing alloy. The gravimetric capacity decreases with the addition of Nb likely due to the higher molar mass of Nb (92.91 g/mol) compared to Ti and Zr (47.86 and 91.22 g/mol, respectively).

The PCI curves at different temperatures for the  $(\text{Ti}_{0.33}\text{Zr}_{0.33}\text{Nb}_{0.33})_1(\text{Mn}_{0.5}\text{Cr}_{0.5})_2$  alloy are illustrated in Figure 7b. The PCI measurements were performed at 30, 50, and 70 °C up to the maximum hydrogen pressure of 80 bar. The maximum hydrogen uptake at 80 bar decreases as the temperature increases, as expected:  $\text{H}/\text{M} = 0.92$  (1.50 wt %),  $\text{H}/\text{M} = 0.90$  (1.46 wt %), and  $\text{H}/\text{M} = 0.83$  (1.35 wt %), for 30, 50, and 70 °C, respectively. For these temperatures, the observed hydrogen equilibrium pressures for the alloy having  $\text{H}/\text{M} = 0.5$  were approximately 9.6, 15.1, and 26.2 bar, respectively.

Once again, although the proposed thermodynamic model provided a reasonable estimate of the equilibrium pressure for the Nb-containing alloy, the actual equilibrium pressure was found to be lower than the calculated value. Nonetheless, the experimental pressure was considerably higher than the desired 1 bar, allowing for complete desorption, as the hydrogen pressure decreased to 1 bar. This feature can be seen in Figure 7b and further explored in the cycling study presented in Section 3.3.2.

Furthermore, the hydrogen storage capacities observed for the  $(\text{Ti}_{0.33}\text{Zr}_{0.33}\text{Nb}_{0.33})_1(\text{Mn}_{0.5}\text{Cr}_{0.5})_2$  alloy in the kinetics and PCI measurements are slightly lower than the theoretical value of 1.62 wt % calculated considering the formation of an  $\text{AB}_2\text{H}_3$  hydride. This condition should be related primarily to the constraints of the experimental pressure limit around 80 bar. It is possible that the hydrogen uptake would increase if pressure above 80 bar was applied to the sample since this composition presents a higher hydrogen equilibrium pressure compared to the two compositions discussed previously. This pressure limit is also the cause of the decrease in the hydrogen absorption capacity as the temperature increases.

It is important to mention that the PCI curves at the different measured temperatures also exhibited minimal hysteresis for the  $(\text{Ti}_{0.33}\text{Zr}_{0.33}\text{Nb}_{0.33})_1(\text{Mn}_{0.5}\text{Cr}_{0.5})_2$  alloy. Moreover, even with less sloped PCI curves, the absence of a well-defined plateau pressure was also observed in the PCI curves of the  $(\text{Ti}_{0.33}\text{Zr}_{0.33}\text{Nb}_{0.33})_1(\text{Mn}_{0.5}\text{Cr}_{0.5})_2$  alloy. As reported in the literature, experimental PCT diagrams of C14 Laves phase alloys are found in two typical shapes: with a flat plateau region with a well-defined pressure and without a well-defined plateau pressure. These shapes are related to the occurrence or not, respectively, of phase separation between a low hydrogen content solid solution and a high hydrogen content hydride. PCT curves with a well-defined plateau pressure were reported for the Laves phase alloys  $(\text{TiZr})_1(\text{CrMnFeNi})_2$ ,<sup>7</sup>  $\text{Ti}_{1-y}\text{Cr}_{2-x}\text{Mn}_x$ ,<sup>30</sup>  $\text{Ti}_{0.8}\text{Zr}_{0.2}\text{Mn}_{0.9}\text{Cr}_{0.6}\text{V}_{0.3}\text{M}_{0.2}$  ( $\text{M} = \text{Fe}, \text{Ni}, \text{and Co}$ ),<sup>17</sup> and  $(\text{Ti}_{0.8}\text{Zr}_{0.2})_{1.1}\text{Mn}_{1.2}\text{Cr}_{0.55}\text{Ni}_{0.2}\text{V}_{0.05}$ .<sup>29</sup> In contrast, the absence of a well-defined plateau pressure suggests hydrogen absorption only by interstitial solid solution. This behavior was reported for  $\text{Ti}_{20}\text{Zr}_{20}\text{Nb}_5\text{Fe}_{40}\text{Ni}_{15}$ ,<sup>22</sup>  $\text{Ti}_{0.5}\text{Zr}_{0.5}\text{V}_{0.5}\text{Ni}_{1.1}\text{Mn}_{0.2}\text{Fe}_{0.2}$ ,<sup>31</sup>  $\text{Cr}_u\text{Fe}_v\text{Mn}_w\text{Ti}_x\text{V}_y\text{Zr}_z$ ,<sup>32</sup> and  $(\text{Ti}_{0.5}\text{Zr}_{0.5})_1(\text{Fe}_{0.33}\text{Mn}_{0.33}\text{Cr}_{0.33})_2$  alloys with the predominant presence of the C14 Laves phase.

**3.3.2. Reversibility and Cycling Performance.** The hydrogen absorption/desorption cycling performance of the



$(\text{Ti}_{0.5}\text{Zr}_{0.5})_1(\text{Mn}_{0.5}\text{Cr}_{0.5})_2$  and  $(\text{Ti}_{0.33}\text{Zr}_{0.33}\text{Nb}_{0.33})_1(\text{Mn}_{0.5}\text{Cr}_{0.5})_2$  alloys was evaluated by measuring the hydrogen absorption capacity over different cycling procedures. The hydrogen absorption/desorption performance of the  $(\text{Ti}_{0.5}\text{Zr}_{0.5})_1(\text{Mn}_{0.5}\text{Cr}_{0.5})_2$  alloy was initially evaluated by measuring the hydrogen absorption/desorption capacity over 20 cycles at 30 °C. The results of the cycling test are shown in Figure 8a, where it is possible to see the hydrogen absorption

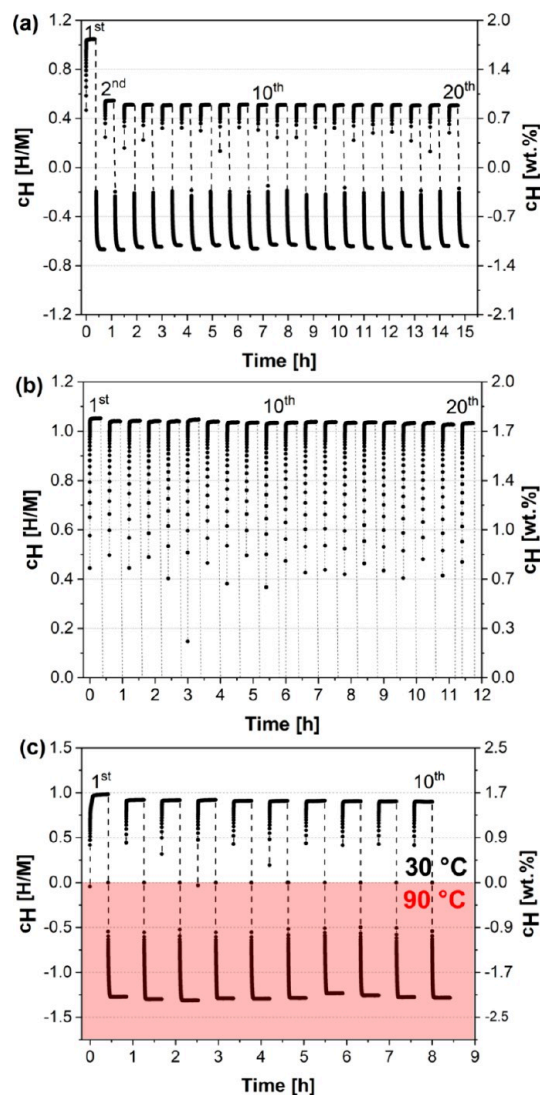


**Figure 8.** Hydrogen absorption capacity in H/M and wt % for  $(\text{Ti}_{0.5}\text{Zr}_{0.5})_1(\text{Mn}_{0.5}\text{Cr}_{0.5})_2$  alloy. (a) Over 20 absorption/desorption cycles at 30 °C with desorption at 0.3 bar (no vacuum). (b) Over 20 absorption cycles at 30 °C with desorption under a dynamic vacuum. (c) Over 10 cycles with absorption at 30 °C and desorption at 90 °C and 0.2 bar (no vacuum). During all absorptions, the initial hydrogen pressure was 21 bar, and the final pressure was 16 bar, approximately.

and desorption curves for all 20 cycles. The hydrogen absorption behavior was investigated at 30 °C under an initial pressure of 21 bar for 20 min, while hydrogen desorption was performed at the same temperature with an initial pressure of approximately 0.3 bar for 20 min. In the first cycle, the hydrogen absorption capacity was  $\text{H/M} = 1.05$  (1.76 wt %), which decreased to  $\text{H/M} = 0.54$  (0.93 wt %) in the second cycle. Following the second cycle, a slight reduction in hydrogen absorption was observed in the subsequent cycles,

stabilizing at  $\text{H/M} = 0.50$  (0.86 wt %). This suggests that the alloy retains its storage capacity after the second cycle. It is important to note that the sample was not subjected to dynamic vacuum conditions during the dehydrogenation kinetics measurements. Therefore, the observed decrease in hydrogen absorption capacity can be attributed to the residual hydrogen retained in the alloy during the cycling process. Moreover, we must stress that as the desorption measurement is performed in the large reservoir volume, the desorption capacity is estimated by small variation of pressure, which considerably increases the error in the desorption capacity.

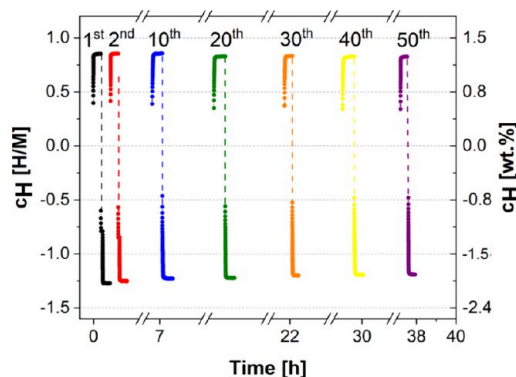
Two additional cycling experiments were conducted to evaluate the reversibility of the alloy. To determine whether the decrease in hydrogen capacity observed in Figure 8a was due to residual hydrogen in the sample holder, desorption was performed under a dynamic vacuum. As shown in Figure 8b, the hydrogen absorption capacity remained nearly constant over 20 cycles. In the first cycle, the hydrogen absorption capacity was  $\text{H/M} = 1.05$  (1.77 wt %), and in the second cycle, it was  $\text{H/M} = 1.04$  (1.75 wt %). No significant decrease in hydrogen absorption was observed over the subsequent cycles. By the 20th cycle, the capacity was  $\text{H/M} = 1.03$  (1.74 wt %), indicating that the alloy retained 98% of its initial hydrogen storage capacity over 20 cycles.

Figure 8c illustrates a different cycling methodology that was carried out. During the absorption cycles, the temperature was maintained at 30 °C with an initial hydrogen pressure of 21 bar. For desorption, the sample temperature was increased to 90 °C while the sample holder was kept closed. The desorption kinetics were carried out by reducing the hydrogen pressure in the sample to below 1 bar over a period of 20 min. To achieve pressures below 1 bar, the hydrogen gas was expanded into the apparatus's largest volume reservoir (1040 cm<sup>3</sup>). The alloy was subjected to 10 absorption/desorption cycles.

A temperature of 90 °C was selected to overcome the barrier to complete desorption without requiring a vacuum. As shown in the PCT diagram (Figure 7a), at 30 °C, the equilibrium pressure is near the atmospheric pressure (0.43 bar), indicating that desorption would be incomplete when the hydrogen pressure is near the ambient pressure. This behavior is depicted by the yellowish region in Figure 7a. Specifically, during absorption at 20 bar, the alloys exhibit an absorption capacity of 1.84 wt % (1.09 H/M), while during desorption at 0.3 bar, the alloy retains 0.81 wt % (0.56 H/M) of hydrogen. In contrast, the PCT diagram indicates that at 90 °C, the equilibrium pressure of the alloy rises to 3.5 bar, which would facilitate the desorption. Therefore, even without exposing the sample to a dynamic vacuum, the alloy is expected to desorb nearly completely when the hydrogen pressure is reduced to approximately 1 bar. This condition is illustrated by the yellowish plus reddish rectangle in Figure 7a, i.e., during the desorption at 90 °C, the alloy desorbs almost completely when the pressure reaches 0.2 bar. The maximum hydrogen absorption capacity in the first cycle was  $\text{H/M} = 1.01$  (1.70 wt %), which decreased to  $\text{H/M} = 0.92$  (1.55 wt %) in the second cycle and further to  $\text{H/M} = 0.90$  (1.51 wt %) over the next eight cycles. This trend indicates that the alloy demonstrates good reversibility in its hydrogen storage properties. The ability to desorb without the need for dynamic vacuum application represents a key advantage for practical applications, making this methodology a viable alternative for effective hydrogen storage under mild pressure and temperature conditions.

It is worth noting that in Figures 8a,c, the desorption capacity exceeds that of absorption. This difference is related to a set of factors that occur during the cycling tests. Initially, there exists a difference in the volumes of the reservoirs used during the absorption and desorption measurements. For absorption, the reservoir volume ranged between 11 and 13 cm<sup>3</sup>, whereas during desorption, the gas was expanded into a reservoir with a volume of 1040 cm<sup>3</sup>. Furthermore, calibration of the larger volume reservoir was not conducted prior to cycling tests. Additionally, a transition from the high-pressure sensor (associated with the smaller volume reservoir) to the low-pressure sensor (linked to the larger volume reservoir) occurs during desorption. Therefore, the higher capacity measured during desorption must be seen as an artifact of the measurement, and the real reversible capacity of the alloy must be considered those measured in absorption measurements.

Regarding the (Ti<sub>0.33</sub>Zr<sub>0.33</sub>Nb<sub>0.33</sub>)<sub>1</sub>(Mn<sub>0.5</sub>Cr<sub>0.5</sub>)<sub>2</sub> alloy, the hydrogen absorption and desorption cycling performance was evaluated by measuring its hydrogen absorption capacity over 50 cycles. The hydrogen absorption measurement was carried out at 30 °C under an initial pressure of 36 bar for 20 min, while the hydrogen desorption was carried out at the same temperature under an initial pressure of approximately 0.4 bar for 20 min. Figure 9 shows the hydrogen absorption and



**Figure 9.** Hydrogen absorption capacity in H/M of the (Ti<sub>0.33</sub>Zr<sub>0.33</sub>Nb<sub>0.33</sub>)<sub>1</sub>(Mn<sub>0.5</sub>Cr<sub>0.5</sub>)<sub>2</sub> alloy over the 1st, 2nd, 10th, 20th, 30th, 40th, and 50th cycles of absorption/desorption. During the absorption, the initial pressure was 36 bar and the final pressure was 34 bar, approximately; the desorption was carried under an initial pressure of 0.4 bar, without vacuum exposure.

desorption curves for the 1st, 2nd, 10th, 20th, 30th, 40th, and 50th cycles. The hydrogen absorption capacity in the first cycle was H/M = 0.85 (1.38 wt %), and no decrease in the capacity was observed until the 10th cycle. A slight decrease in hydrogen absorption was observed during the subsequent cycles until H/M = 0.82 (1.33 wt %) in the 50th cycle. It is worth noting that a higher reversible capacity could be attained if a higher absorption pressure, for instance, 80 bar, was applied.

The observed slight reduction in hydrogen storage capacity over the cycles for the (Ti<sub>0.33</sub>Zr<sub>0.33</sub>Nb<sub>0.33</sub>)<sub>1</sub>(Mn<sub>0.5</sub>Cr<sub>0.5</sub>)<sub>2</sub> alloy can be attributed to residual hydrogen remaining in the alloy and sample holder during cycling since the sample was not subjected to a dynamic vacuum during the dehydrogenation kinetics measurement.

Nevertheless, the cycling results demonstrate that the alloy retains at least 96% of its initial capacity after 50 cycles,

indicating that it possesses excellent reversible hydrogen storage properties. For this alloy, no increase in temperature or vacuum was required to perform the cycling experiments since the PCT diagram (Figure 7b) showed that the sample could be desorbed almost entirely (H/M < 0.1) by reducing the hydrogen pressure to approximately 1 bar, even at 30 °C. The yellowish rectangle in Figure 7b highlights the pressure and capacity ranges observed during this test.

Figure 10 presents the XRD patterns of both alloys under three conditions: as-cast, after one absorption cycle, and after

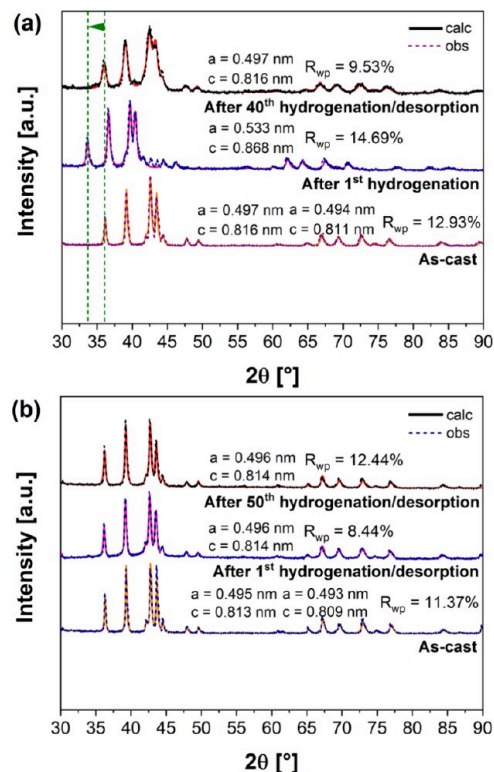


**Figure 10.** XRD patterns of the (a) (Ti<sub>0.5</sub>Zr<sub>0.5</sub>)<sub>1</sub>(Mn<sub>0.5</sub>Cr<sub>0.5</sub>)<sub>2</sub> and (b) (Ti<sub>0.33</sub>Zr<sub>0.33</sub>Nb<sub>0.33</sub>)<sub>1</sub>(Mn<sub>0.5</sub>Cr<sub>0.5</sub>)<sub>2</sub> alloys in the as-cast, after one absorption/desorption cycle, and after 40 absorption/desorption cycles conditions.

40 or 50 cycles. Figure 10a presents the XRD patterns and lattice parameters obtained by Rietveld refinement for the C14 Laves phase under these three conditions for the (Ti<sub>0.5</sub>Zr<sub>0.5</sub>)<sub>1</sub>(Mn<sub>0.5</sub>Cr<sub>0.5</sub>)<sub>2</sub> alloy.

One can see that after one and 40 hydrogenation cycles, the (Ti<sub>0.5</sub>Zr<sub>0.5</sub>)<sub>1</sub>(Mn<sub>0.5</sub>Cr<sub>0.5</sub>)<sub>2</sub> samples still presented a single C14 Laves phase. However, changes in the lattice parameters were observed. As discussed above, if this alloy has a hydrogen equilibrium pressure lower than 1 bar, then it is not able to desorb completely without dynamic vacuum exposure. To characterize the hydride, the sample was not desorbed following initial exposure to hydrogen. Instead, the sample was sent for XRD characterization immediately after the hydrogenation experiment was completed. Thus, a shift to the left of the C14 phase reflections was observed, as indicated by the arrow and dashed green lines. This shift to the left is a consequence of an increase in the lattice parameters of the C14 Laves phase structure, which increased from  $a = 0.497$  and  $c = 0.816$  nm to  $a = 0.533$  and  $c = 0.868$  nm. In terms of unit cell volume, it corresponds to an increase from 174.56 to 213.39 Å<sup>3</sup>



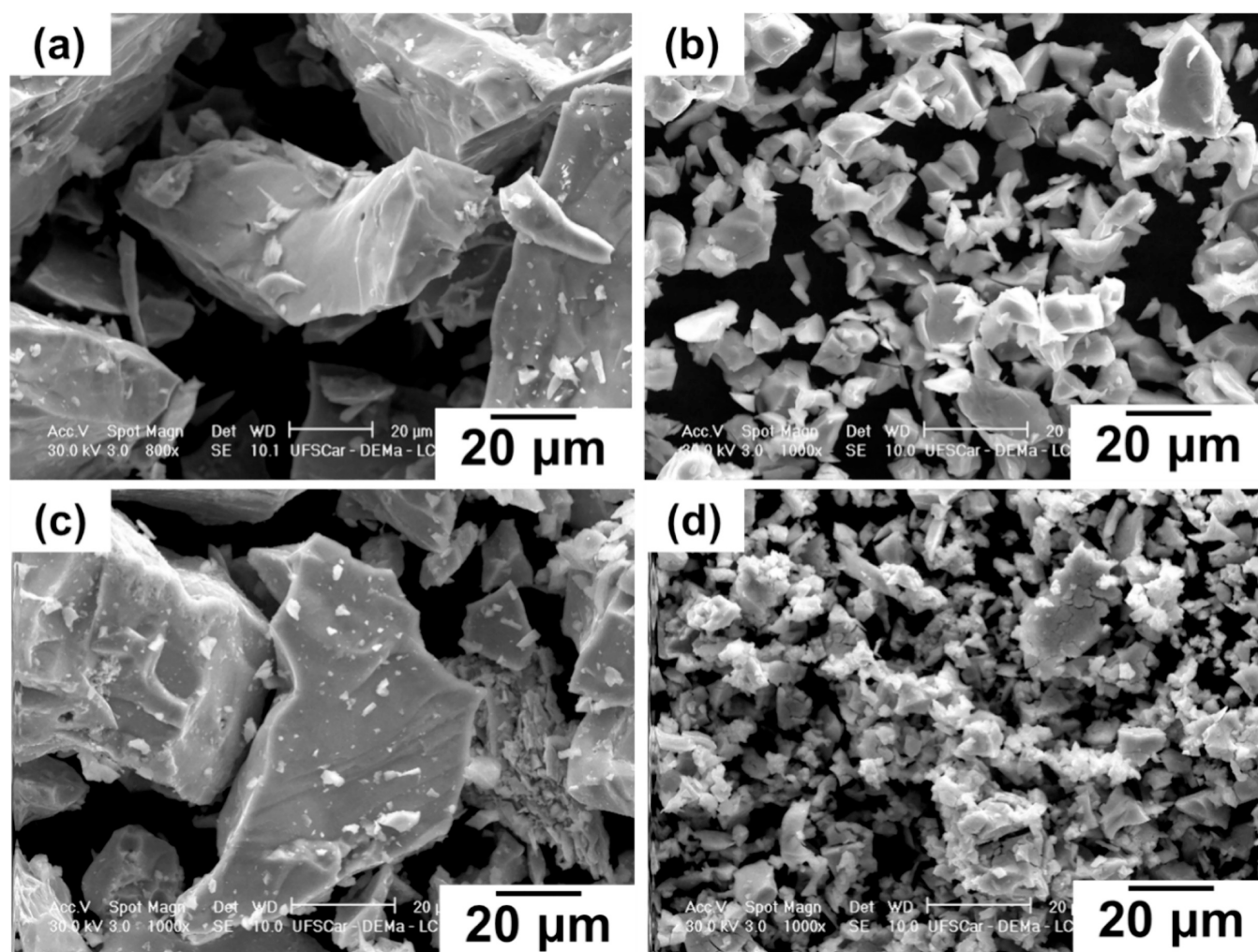


**Figure 11.** SEM images of the  $(\text{Ti}_{0.5}\text{Zr}_{0.5})_1(\text{Mn}_{0.5}\text{Cr}_{0.5})_2$  alloy (a) prior to the hydrogenation test and (b) after the 40th cycles of hydrogenation/dehydrogenation and of the  $(\text{Ti}_{0.33}\text{Zr}_{0.33}\text{Nb}_{0.33})_1(\text{Mn}_{0.5}\text{Cr}_{0.5})_2$  alloy (c) prior to the hydrogenation tests and (d) after the 50th cycles of hydrogenation/dehydrogenation.

(or from 14.54 to 17.83 Å<sup>3</sup> per metal atom). According to the well-known Peisl relationship,<sup>33</sup> this volume expansion corresponds to a hydrogen uptake of 1.13 H/M if an hydrogen volume of 2.9 Å<sup>3</sup> is considered, as proposed by Peisl. This is also consistent with the capacity observed in the kinetic measurement (Figure 6a), which was performed prior to the XRD analysis. Furthermore, the diffraction pattern of the sample after 40 absorption/desorption cycles showed no significant change in lattice parameters, as it underwent a desorption measurement prior to XRD analysis. However, peak broadening was observed in this sample. This broadening may be attributed to variations in lattice parameters across different crystals or to an increase in crystalline defects, such as dislocations and grain boundaries, which develop during the hydrogenation cycles.

Figure 10b presents the XRD patterns of the  $(\text{Ti}_{0.33}\text{Zr}_{0.33}\text{Nb}_{0.33})_1(\text{Mn}_{0.5}\text{Cr}_{0.5})_2$  alloy under the same three conditions. As observed, no changes in the constituent phases were detected, even after multiple hydrogenation cycles. Following one and 50 hydrogenation/dehydrogenation cycles, the samples exhibited a single C14 Laves phase, with no observable changes in lattice parameters. These XRD results, together with the PCT diagram and cycling measurements, suggest that the  $(\text{Ti}_{0.33}\text{Zr}_{0.33}\text{Nb}_{0.33})_1(\text{Mn}_{0.5}\text{Cr}_{0.5})_2$  alloy effi-

ciently desorbs completely when the pressure is reduced to 1 bar. Furthermore, hydrogen retained in the alloy structure was released during the sample evacuation prior to further characterization. As a result, XRD analysis of the hydrogenated phase was not possible after the hydrogenation tests.

Figure 11 illustrates the powder characteristics of the  $(\text{Ti}_{0.5}\text{Zr}_{0.5})_1(\text{Mn}_{0.5}\text{Cr}_{0.5})_2$  and  $(\text{Ti}_{0.33}\text{Zr}_{0.33}\text{Nb}_{0.33})_1(\text{Mn}_{0.5}\text{Cr}_{0.5})_2$  alloys under two conditions. Figure 11a,c shows the powder morphologies of the  $(\text{Ti}_{0.5}\text{Zr}_{0.5})_1(\text{Mn}_{0.5}\text{Cr}_{0.5})_2$  and  $(\text{Ti}_{0.33}\text{Zr}_{0.33}\text{Nb}_{0.33})_1(\text{Mn}_{0.5}\text{Cr}_{0.5})_2$  alloys, respectively, after they were crushed into powder for loading into the Sieverts-type apparatus. The particle sizes of both alloys are approximately 200 μm. Figure 11b,d shows the samples after 40 or 50 cycles of hydrogen absorption and desorption. A noticeable reduction in particle size is observed, along with the development of surface cracks. This behavior has been reported in previous studies and is attributed to volume expansion of the C14 Laves phase during hydrogen absorption. This expansion induces significant internal stress within the host metal, leading to its embrittlement postabsorption. As a result, the alloy forms a powder with fine particle sizes ranging from 10 to 100 μm.<sup>1,17,34</sup> As previously mentioned, the reduction in alloy particle size by at least 1 order of magnitude leads to an increase in crystalline defects, such as dislocations

and grain boundaries. This contributes to peak broadening in the XRD patterns, as observed for the alloys.

### 3.4. Potential Applications of the Investigated Alloys.

This work highlights the storage capacity and reversibility of C14-type Laves phase alloys. Ongoing research and development efforts are focused on expanding their applications, including hydrogen storage tanks, thermal energy storage systems, purification and separation technologies, fuel cells, batteries, and vehicles.

Of the applications listed above, the transportation sector holds the greatest potential for expanding the use of hydrogen-based energy systems. Additionally, in the absence of poisonous substances ( $O_2$  and  $H_2O$ ), metal hydrides can serve as highly effective materials for gas purification and storage. They can selectively absorb and store hydrogen from a mixture of gases, making them ideal for such applications.<sup>35</sup>

Regarding the transport sector, concerns over resource depletion and fossil fuel impacts have driven the development of hydrogen-powered vehicles. Toyota's research team demonstrated the utilization of  $Ti_{1.1}MnCr$  alloys in high-pressure metal hydride tanks, achieving 1.9 wt % hydrogen storage at 350 bar in 2006.<sup>36</sup> Later, in 2015, they introduced fuel-cell vehicles with 700-bar high-pressure metal hydride tanks delivering 5.7 wt % hydrogen density.<sup>37</sup> However, high operating pressures pose safety and cost challenges, highlighting the potential of room-temperature hydrogen storage tanks for safer, cost-effective energy solutions.

Regarding the process of hydrogen separation and purification, the use of metal hydrides relies on the selective adsorption properties of hydrogen storage materials. The metal hydride method offers advantages over other hydrogen separation techniques, including a straightforward system design, low energy consumption, safe and simple operation, and a high hydrogen recovery rate. For example, cryogenic separation requires significant amounts of liquid nitrogen and involves a substantial capital investment. Similarly, the palladium membrane adsorption method is limited in its ability to remove impurities such as  $N_2$  and  $CH_4$ . Additionally, the palladium tubes used in membrane separation are not only costly but also prone to contamination, which can reduce their effectiveness over time.<sup>38</sup> Chen et al.<sup>38</sup> reported in their review paper the use of ammonia process exhaust gas to recover hydrogen using an  $AB_5$ -type alloy. A hydrogen recovery rate of 81–86% was achieved, with the resulting hydrogen product reaching a purity of 99.9%. However, proper heat management during hydrogen absorption and desorption is essential for facilitating fast and complete reactions. Additionally, Dunikov et al.<sup>39</sup> demonstrated that hydrogen purification is highly dependent on a low equilibrium pressure to achieve efficient purification and high recovery rates. Their study, which involved an  $AB_5$ -type alloy with an equilibrium pressure of 0.38 bar at 20 °C, highlighted this factor.  $AB_2$ -type alloys are promising materials for hydrogen purification due to their ability to readily absorb hydrogen.<sup>40</sup>

The challenges presented above align directly with the core focus of this work: optimizing compositions to achieve the specific properties required for targeted applications. The  $(Ti_{0.33}Zr_{0.33}Nb_{0.33})_1(Mn_{0.5}Cr_{0.5})_2$  alloy, for example, shows significant potential as a material for room-temperature hydrogen storage in both mobile and stationary applications. As previously discussed, this alloy has a hydrogen equilibrium pressure of approximately 10 bar at 30 °C, allowing it to absorb hydrogen at moderate pressures and release it at room

temperature under atmospheric pressure. On the other hand, the  $(Ti_{0.5}Zr_{0.5})_1(Mn_{0.5}Cr_{0.5})_2$  alloy, could be suitable for hydrogen separation and purification. As demonstrated in this work, the hydrogenation reaction in metals and alloys is reversible under certain conditions that depend on the host metal. Typically, pressurization or cooling facilitates the formation of metal hydrides, while heating or decompression promotes the release of hydrogen during the reverse reaction. Therefore, the  $(Ti_{0.5}Zr_{0.5})_1(Mn_{0.5}Cr_{0.5})_2$  alloy, with its equilibrium pressure of 0.43 bar at 30 °C, can easily absorb hydrogen at temperatures near room temperature and fully desorb when the temperature is increased to around 90 °C, allowing its application in H purification systems operating in mild temperature conditions. Furthermore, this alloy could be a promising candidate for use in Ni-MH batteries. For this application, the equilibrium pressure at room-temperature should remain between 0.1 and 1 atm to minimize self-discharge and prevent the internal pressure of the battery from exceeding atmospheric levels.<sup>41</sup>

## 4. CONCLUSIONS

This study demonstrated the significant potential of C14 Laves phase alloys for solid-state hydrogen storage as a promising alternative to expand the use of hydrogen energy systems and accelerate the transition to renewable energy sources. This study systematically investigated two compositions from the  $(Ti_{0.5-x}Zr_{0.5-x}Nb_{2x})_1(Mn_{0.5}Cr_{0.5})_2$  alloy system:  $(Ti_{0.5}Zr_{0.5})_1(Mn_{0.5}Cr_{0.5})_2$  and  $(Ti_{0.33}Zr_{0.33}Nb_{0.33})_1(Mn_{0.5}Cr_{0.5})_2$  alloys, corresponding to  $x = 0$  and 0.1667, respectively.

The applied thermodynamic computational approach enabled the design of these multicomponent alloys with optimized hydrogen storage properties. Although the  $(Ti_{0.5}Zr_{0.5})_1(Mn_{0.5}Cr_{0.5})_2$  alloy exhibited incomplete desorption at 30 °C, due to its low hydrogen equilibrium pressure ( $\sim 0.4$  bar), an effective solution was proposed using temperature-induced desorption at 90 °C, overcoming this limitation and offering a viable option for large-scale storage. Furthermore, the  $(Ti_{0.33}Zr_{0.33}Nb_{0.33})_1(Mn_{0.5}Cr_{0.5})_2$  alloy demonstrated an exceptional reversible hydrogen storage capacity under ambient temperature and moderate pressure conditions. This performance was attributed to the increased equilibrium pressure ( $\sim 10$  bar) resulting from the addition of Nb.

In addition to their excellent reversible hydrogen storage properties under moderate pressure and temperature conditions, both alloys exhibited fast kinetics, reaching their full absorption capacity in under a minute. Further structural analysis of the alloys after multiple hydrogenation-dehydrogenation cycles confirmed the stability of the single C14 Laves phase and the consistency of its lattice parameters over cycling.

## ■ ASSOCIATED CONTENT

### Supporting Information

The following files are available free of charge. The Supporting Information is available free of charge at <https://pubs.acs.org/doi/10.1021/acsaem.5c00876>.

Calculated hydrogen equilibrium pressures and PCI curves at 25 °C for the  $(Ti_{0.5-x}Zr_{0.5-x}Nb_{2x})_1(Mn_{0.5}Cr_{0.5})_2$  system alloys for  $x = 0$  to  $x = 0.5$  as well as unit cell and crystal structure of the hexagonal C14 Laves phase for the  $(Ti_{0.5}Zr_{0.5})_1(Mn_{0.5}Cr_{0.5})_2$  and  $(Ti_{0.33}Zr_{0.33}Nb_{0.33})_1(Mn_{0.5}Cr_{0.5})_2$  alloys (PDF)



## AUTHOR INFORMATION

## Corresponding Author

Jéssica Bruna Ponsoni – Department of Materials Engineering (DEMa/UFSCar) - Rodovia Washington Luiz, km 235, Federal University of São Carlos, São Carlos, SP 13565-905, Brazil; [orcid.org/0000-0003-0001-6689](https://orcid.org/0000-0003-0001-6689); Email: [jessicaponsoni@estudante.ufscar.br](mailto:jessicaponsoni@estudante.ufscar.br)

## Authors

Vinicius Aranda – Graduate Program in Materials Science and Engineering (PPGCEM/UFSCar) - Rodovia Washington Luiz, km 235, Federal University of São Carlos, São Carlos, SP 13565-905, Brazil

Walter J. Botta – Department of Materials Engineering (DEMa/UFSCar) - Rodovia Washington Luiz, km 235 and Graduate Program in Materials Science and Engineering (PPGCEM/UFSCar) - Rodovia Washington Luiz, km 235, Federal University of São Carlos, São Carlos, SP 13565-905, Brazil

Guilherme Zepon – Department of Materials Engineering (DEMa/UFSCar) - Rodovia Washington Luiz, km 235 and Graduate Program in Materials Science and Engineering (PPGCEM/UFSCar) - Rodovia Washington Luiz, km 235, Federal University of São Carlos, São Carlos, SP 13565-905, Brazil; [orcid.org/0000-0002-5852-9076](https://orcid.org/0000-0002-5852-9076)

Complete contact information is available at: <https://pubs.acs.org/10.1021/acsaem.5c00876>

## Funding

The Article Processing Charge for the publication of this research was funded by the Coordenacao de Aperfeiçoamento de Pessoal de Nível Superior (CAPES), Brazil (ROR identifier: 00x0ma614).

## Notes

The authors declare no competing financial interest.

## ACKNOWLEDGMENTS

This work was financed in part by Brazilian National Council for Scientific and Technological Development – CNPq (grant numbers: 381973/2023-9, 309467/2021-7, and 407906/2022-3), in part by the Serrapilheira Institute (grant number Serra-1709-17362), and in part by the Studies and Project Funding, FINEP (grant number: FINEP 01.22.0177.00). This study was also financed in part by the Coordenação de Aperfeiçoamento de Pessoal de Nível Superior – Brasil (CAPES) – Finance Code 001, Federal University of São Carlos, Graduate Program in Materials Science and Engineering. The authors would like to acknowledge Structural Characterization Laboratory – LCE at Federal University of São Carlos – UFSCAR for the electron microscopy and x-ray diffraction facilities.

## REFERENCES

- (1) Züttel, A. Materials for Hydrogen Storage. *Mater. Today* **2003**, *6*, 24–33.
- (2) Marques, F.; Balcerzak, M.; Winkelmann, F.; Zepon, G.; Felderhoff, M. Review and Outlook on High-Entropy Alloys for Hydrogen Storage. *Energy Environ. Sci.* **2021**, *14* (10), 5191–5227.
- (3) Schlapbach, L.; Züttel, A. Hydrogen-Storage Materials for Mobile Applications. *Nature* **2001**, 353.
- (4) Marinelli, M.; Santarelli, M. Hydrogen Storage Alloys for Stationary Applications. *J. Energy Storage* **2020**, *32*, No. 101864.
- (5) Mayer Dias, G. C.; Silva, B. H.; De Sousa Martins, A.; Felderhoff, M.; Botta, W. J.; Zepon, G. Hydride Destabilization in the Ti–Nb–Cr System Through Nb/Ti Ratio Adjustment. *ACS Appl. Energy Mater.* **2024**, *7* (15), 6463–6474.
- (6) Kohlmann, H. Hydrogen Order in Hydrides of Laves Phases. *Z. Für Krist. - Cryst. Mater.* **2020**, *235* (8–9), 319–332.
- (7) Edalati, P.; Floriano, R.; Mohammadi, A.; Li, Y.; Zepon, G.; Li, H. W.; Edalati, K. Reversible Room Temperature Hydrogen Storage in High-Entropy Alloy TiZrCrMnFeNi. *Scr. Mater.* **2020**, *178*, 387–390.
- (8) Ponsoni, J. B.; Balcerzak, M.; Botta, W. J.; Felderhoff, M.; Zepon, G. A Comprehensive Investigation of the  $(\text{Ti}_{0.5}\text{Zr}_{0.5})_1(\text{Fe}_{0.33}\text{Mn}_{0.33}\text{Cr}_{0.33})_2$  Multicomponent Alloy for Room-Temperature Hydrogen Storage Designed by Computational Thermodynamic Tools. *J. Mater. Chem. A* **2023**, *11* (26), 14108–14118.
- (9) Stein, F.; Leineweber, A. Laves Phases: A Review of Their Functional and Structural Applications and an Improved Fundamental Understanding of Stability and Properties. *J. Mater. Sci.* **2021**, *56* (9), 5321–5427.
- (10) Ma, P.; Li, W.; Wu, E. Hydrogen Activation and Storage Properties of Laves Phase Ti1-Sc Mn1.6V0.4 Alloys. *Int. J. Hydrog. Energy* **2021**, *46* (69), 34389–34398.
- (11) Guo, X.; Wang, S.; Liu, X.; Li, Z.; Lü, F.; Mi, J.; Hao, L.; Jiang, L. Laves Phase Hydrogen Storage Alloys for Super-High-Pressure Metal Hydride Hydrogen Compressors. *Rare Met.* **2011**, *30* (3), 227–231.
- (12) Peng, Z.; Li, Q.; Sun, J.; Chen, K.; Jiang, W.; Wang, H.; Liu, J.; Ouyang, L.; Zhu, M. Ti–Cr–Mn–Fe–Based Alloys Optimized by Orthogonal Experiment for 85 MPa Hydrogen Compression Materials. *J. Alloys Compd.* **2022**, *891*, No. 161791.
- (13) Kandavel, M.; Bhat, V. V.; Rougier, A.; Aymard, L.; Nazri, G.-A.; Tarascon, J.-M. Improvement of Hydrogen Storage Properties of the AB<sub>2</sub> Laves Phase Alloys for Automotive Application. *Int. J. Hydrog. Energy* **2008**, *33* (14), 3754–3761.
- (14) Chen, H.; Yu, H.; Zhang, Q.; Liu, B.; Liu, P.; Zhou, X.; Han, Z.; Zhou, S. Enhancement in Dehydrogenation Performance of Magnesium Hydride by Iron Incorporation: A Combined Experimental and Theoretical Investigation. *J. Power Sources* **2016**, *322*, 179–186.
- (15) Liu, P.; Xie, X.; Xu, L.; Li, X.; Liu, T. Hydrogen Storage Properties of (Ti 0.85 Zr 0.15) 1.05 Mn 1.2 Cr 0.6 V 0.1 M 0.1 (M = Ni, Fe, Cu) Alloys Easily Activated at Room Temperature. *Prog. Nat. Sci. Mater. Int.* **2017**, *27* (6), 652–657.
- (16) Bobet, J. Relationship between Hydrogen Sorption Properties and Crystallography for TiMn<sub>2</sub> Based Alloys. *Int. J. Hydrog. Energy* **2000**, *25* (8), 767–772.
- (17) Li, Z.; Yan, Y.; Huang, H.; Liu, B.; Lv, Y.; Zhang, B.; Lv, W.; Yuan, J.; Wu, Y. Effects of the Different Element Substitution on Hydrogen Storage Properties of Ti<sub>0.8</sub>Zr<sub>0.2</sub>Mn<sub>0.9</sub>Cr<sub>0.6</sub>V<sub>0.3</sub>M<sub>0.2</sub> (M = Fe, Ni, Co). *J. Alloys Compd.* **2022**, *908*, No. 164605.
- (18) Ponsoni, J. B.; Aranda, V.; Nascimento, T. da S.; Strozi, R. B.; Botta, W. J.; Zepon, G. Design of Multicomponent Alloys with C14 Laves Phase Structure for Hydrogen Storage Assisted by Computational Thermodynamic. *Acta Mater.* **2022**, *240*, No. 118317.
- (19) Zepon, G.; Silva, B. H.; Zlotea, C.; Botta, W. J.; Champion, Y. Thermodynamic Modelling of Hydrogen-Multicomponent Alloy Systems: Calculating Pressure-Composition-Temperature Diagrams. *Acta Mater.* **2021**, *215*, No. 117070.
- (20) Mishra, S. S.; Yadav, T. P.; Srivastava, O. N.; Mukhopadhyay, N. K.; Biswas, K. Formation and Stability of C14 Type Laves Phase in Multi Component High-Entropy Alloys. *J. Alloys Compd.* **2020**, *832*, No. 153764.
- (21) Xian, Y.; Zheng, H.; Zhai, Q.; Luo, Z. A Two-Dimensional Structure Map for Prediction of the Transition-Metal Laves Phases. *Comput. Mater. Sci.* **2016**, *125*, 1–7.
- (22) Floriano, R.; Zepon, G.; Edalati, K.; Fontana, G. L. B. G.; Mohammadi, A.; Ma, Z.; Li, H.-W.; Contieri, R. J. Hydrogen Storage in TiZrNbFeNi High Entropy Alloys, Designed by Thermodynamic Calculations. *Int. J. Hydrog. Energy* **2020**, *45* (58), 33759–33770.
- (23) Griessen, R.; Riesterer, T. Heat of Formation Models. In *Hydrogen in Intermetallic Compounds I*; Schlapbach, L., Ed.; Topics in

Applied Physics; Springer Berlin Heidelberg: Berlin, Heidelberg, 1988; Vol. 63, pp 219–284. .

(24) Toby, B. H.; Von Dreele, R. B. GSAS-II: The Genesis of a Modern Open-Source All Purpose Crystallography Software Package. *J. Appl. Crystallogr.* **2013**, 46 (2), 544–549.

(25) Hessel Silva, B.; Botta, W. J.; Zepon, G. Design of a Ti–V–Nb–Cr Alloy with Room Temperature Hydrogen Absorption/Desorption Reversibility. *Int. J. Hydrog. Energy* **2023**, 48 (84), 32813–32825.

(26) Silva, B. H.; Zlotea, C.; Champion, Y.; Botta, W. J.; Zepon, G. Design of TiVNb-(Cr, Ni or Co) Multicomponent Alloys with the Same Valence Electron Concentration for Hydrogen Storage. *J. Alloys Compd.* **2021**, 865, No. 158767.

(27) Andrade, G.; Zepon, G.; Edalati, K.; Mohammadi, A.; Ma, Z.; Li, H.-W.; Floriano, R. Crystal Structure and Hydrogen Storage Properties of AB-Type TiZrNbCrFeNi High-Entropy Alloy. *Int. J. Hydrog. Energy* **2023**, 48 (36), 13555–13565.

(28) Zhou, L.; Li, W.; Hu, H.; Zeng, H.; Chen, Q. Ce-Doped TiZrCrMn Alloys for Enhanced Hydrogen Storage. *Energy Fuels* **2022**, 36 (7), 3997–4005.

(29) Tu, B.; Wang, H.; Wang, Y.; Li, R.; Ouyang, L.; Tang, R. Optimizing Ti–Zr–Cr–Mn–Ni–V Alloys for Hybrid Hydrogen Storage Tank of Fuel Cell Bicycle. *Int. J. Hydrog. Energy* **2022**, 47 (33), 14952–14960.

(30) Charbonnier, V.; Enoki, H.; Asano, K.; Kim, H.; Sakaki, K. Tuning the Hydrogenation Properties of Ti1+Cr2-Mn Laves Phase Compounds for High Pressure Metal-Hydride Compressors. *Int. J. Hydrog. Energy* **2021**, 46 (73), 36369–36380.

(31) Akiba, E.; Iba, H. Hydrogen Absorption by Laves Phase Related BCC Solid Solution. *Intermetallics* **1998**, 6 (6), 461–470.

(32) Chen, S.-K.; Lee, P.-H.; Lee, H.; Su, H.-T. Hydrogen Storage of C14-CrFeV<sub>2</sub>MnW<sub>2</sub>Ti<sub>2</sub>V<sub>2</sub>Zr<sub>2</sub> Alloys. *Mater. Chem. Phys.* **2018**, 210, 336–347.

(33) Peisl, H. Lattice Strains Due to Hydrogen in Metals. In *Hydrogen in Metals I*; Alefeld, G.; Völkl, J., Eds.; Amelinckx, S.; Chebotayev, V. P.; Gomer, R.; Ibach, H.; Letokhov, V. S.; Lotsch, H. K. V.; Queisser, H. J.; Schäfer, F. P.; Seeger, A.; Shimoda, K.; Tamir, T.; Welford, W. T.; Wijn, H. P. J., Series Eds.; Topics in Applied Physics; Springer Berlin Heidelberg: Berlin, Heidelberg, 1978; Vol. 28, pp 53–74. .

(34) Dornheim, M. Thermodynamics of Metal Hydrides: Tailoring Reaction Enthalpies of Hydrogen Storage Materials. In *Thermodynamics - Interaction Studies - Solids, Liquids and Gases*; Moreno Piraján, J. C., Ed.; InTech, 2011. .

(35) Miura, S.; Fujisawa, A.; Ishida, M. A Hydrogen Purification and Storage System Using Metal Hydride. *Int. J. Hydrog. Energy* **2012**, 37 (3), 2794–2799.

(36) Kojima, Y.; Kawai, Y.; Towata, S.; Matsunaga, T.; Shinozawa, T.; Kimbara, M. Development of Metal Hydride with High Dissociation Pressure. *J. Alloys Compd.* **2006**, 419 (1–2), 256–261.

(37) Yamashita, A.; Kondo, M.; Goto, S.; Ogami, N. Development of High-Pressure Hydrogen Storage System for the Toyota “Mirai.” SAE Technical Paper 2015–01–11692015.

(38) Chen, X. Y.; Wei, L. X.; Deng, L.; Yang, F. S.; Zhang, Z. X. A Review on the Metal Hydride Based Hydrogen Purification and Separation Technology. *Appl. Mech. Mater.* **2013**, 448–453, 3027–3036.

(39) Dunikov, D.; Borzenko, V.; Blinov, D.; Kazakov, A.; Lin, C.-Y.; Wu, S.-Y.; Chu, C.-Y. Biohydrogen Purification Using Metal Hydride Technologies. *Int. J. Hydrog. Energy* **2016**, 41 (46), 21787–21794.

(40) Koua, K. A. J.; Tong, L.; Yang, T.; Xiao, J. High Purity Hydrogen Production by Metal Hydride System: A Parametric Study Based on the Lumped Parameter Model. *J. Wuhan Univ. Technol.-Mater. Sci. Ed* **2021**, 36 (1), 127–135.

(41) Notten, P. H. L. Rechargeable Nickel-Metalhydride Batteries: A Successful New Concept. In *Interstitial Intermetallic Alloys*; Grandjean, F.; Long, G. J.; Buschow, K. H. J., Eds.; Springer Netherlands: Dordrecht, 1995; pp 151–195. .



CAS BIOFINDER DISCOVERY PLATFORM™

**CAS BIOFINDER  
HELPS YOU FIND  
YOUR NEXT  
BREAKTHROUGH  
FASTER**

Navigate pathways, targets, and  
diseases with precision

**Explore CAS BioFinder**

**CAS**  
A Division of the  
American Chemical Society